ADVANCING EARTH AND SPACE SCIENCE

Earth and Space Science

RESEARCH ARTICLE

10.1029/2021EA002191

Theory of Radar Polarimetric Interferometry and Its Application to the Retrieval of Sea Ice Elevation in the Western Weddell Sea, Antarctic

Son V. Nghiem[1], Lanqing Huang[2], and Irena Hajnsek[2,3]

[1]Jet Propulsion Laboratory, California Institute of Technology, Pasadena, CA, USA, [2]Institute of Environmental Engineering, Swiss Federal Institute of Technology in Zürich (ETH), Zürich, Switzerland, [3]German Aerospace Center (DLR), Microwaves and Radar Institute, Wessling, Germany

Key Points:

- A polarimetric interferometric radar theory is developed based on solutions of Maxwell's equations to calculate Antarctic sea ice elevation
- Theoretical and experimental results are well compared and show an inverse relation between a polarimetric radar term and sea ice elevation
- Based on physical insights from the theory, a protocol is set up to measure elevation of thick and deformed Antarctic sea ice by X band SAR

Correspondence to:

S. V. Nghiem,
son.v.nghiem@jpl.nasa.gov

Citation:

Nghiem, S. V., Huang, L., & Hajnsek, I. (2022). Theory of radar polarimetric interferometry and its application to the retrieval of sea ice elevation in the Western Weddell Sea, Antarctic. *Earth and Space Science*, *9*, e2021EA002191. https://doi.org/10.1029/2021EA002191

Received 21 DEC 2021
Accepted 8 APR 2022

Author Contributions:

Conceptualization: Son V. Nghiem
Data curation: Son V. Nghiem, Lanqing Huang, Irena Hajnsek
Formal analysis: Son V. Nghiem, Lanqing Huang
Funding acquisition: Son V. Nghiem, Irena Hajnsek
Investigation: Son V. Nghiem, Lanqing Huang
Methodology: Son V. Nghiem
Resources: Son V. Nghiem, Irena Hajnsek
Validation: Son V. Nghiem, Lanqing Huang, Irena Hajnsek
Visualization: Son V. Nghiem
Writing – original draft: Son V. Nghiem

Abstract

Sea ice elevation plays a crucial role in sea ice dynamic processes driven by winds and waves, for which satellite radar remote sensing becomes indispensable to monitor snow-covered sea ice across the vast polar regions regardless of darkness and clouds. To measure sea ice elevation, a theory of polarimetric interferometry for both monostatic and bistatic radars is developed based on analytic solutions of Maxwell's equations, accounting for realistic and complicated properties of snow, sea ice, and seawater. This analytic method inherently preserves phase information that is imperative for radar polarimetry and interferometry. Among a multitude of complex radar coefficients in the general polarimetric interferometric covariance matrix, the symmetry group theory is utilized to identify and select appropriate terms pertaining to the retrieval of sea ice elevation while avoiding radar parameters that may inadvertently introduce non-uniqueness and excessive uncertainty. Theoretical calculations compare well with field observations for rough and old sea ice encountered in the Operation-IceBridge and TanDEM-X Antarctic Science Campaign over the Western Weddell Sea. The results show that the magnitude of the coefficient of normalized correlation between co-polarized horizontal and co-polarized vertical radar returns is inversely related to sea ice elevation, while the associate phase term is nonlinear and noisy and should be excluded. From these analyses, a protocol is set up to measure Antarctic sea ice elevation to be presented in the next companion paper.

Plain Language Summary

To understand sea ice processes and advance models for sea ice motions require information on the height of sea ice above the seawater level. For this purpose, an advanced radar theory is developed and validated with measurements from an experiment conducted over Antarctic sea ice. Based on physical insights from the radar theory, a protocol is set up to retrieve the elevation of rough and old sea ice using data acquired by satellite radars for Earth observations.

1. Introduction

Concerning the contrasted behaviors of Arctic and Antarctic sea ice, it becomes crucial to accurately characterize and monitor the state of polar sea ice to explain the differences between Arctic and Antarctic sea ice change, considered by scientists as the polar sea ice paradox (King, 2014; Liu & Curry, 2011; Maksym et al., 2012; Walsh, 2009). Among the parameters critical for sea ice dynamic modeling is the surface elevation to determine the sea ice drag and the momentum flux in air-ice-ocean interactions (Guest & Davidson, 1991). A major weakness is the assumption of a constant sea ice roughness in models, which is overly simplistic and cannot truly capture sea ice dynamic processes (Guest & Davidson, 1991). An advanced study has revealed that it is indeed required to account for variations of sea ice surface elevation in climate simulations in order to correctly represent the implications of sea ice change under a changing climate (Martin et al., 2016).

In the Antarctic, sea ice elevation, including ice freeboard and snow thickness above the local sea level as a reference, is significantly more pronounced than that in the Arctic due to strong wind (e.g., persistent offshore katabatic winds) and wave (e.g., Weddell Gyre driven by Antarctic Circumpolar Current interactions with the Antarctic Continental Shelf) forcing on Antarctic sea ice (Nghiem et al., 2016). Thus, the capability to obtain sea ice digital elevation model (DEM) across the extensive expansion of the sea ice cover is crucial to address the DEM missing gap, especially for Antarctic sea ice. For this objective, the Operation-IceBridge and TanDEM-X Coordinated Science Campaign (OTASC) was successfully conducted in 2017 (Nghiem et al., 2018). This is presented in two

Writing – review & editing: Son V. Nghiem, Lanqing Huang, Irena Hajnsek

consecutive papers: Part 1 for the theory of radar polarimetric interferometry in this paper, and Part 2 for OTASC experimental observations in the next companion paper (Huang et al., 2021).

2. Theoretical Modeling

Understanding sea ice remote sensing signatures was a thrust of the Accelerated Research Initiatives (ARI) in the 1990s, leading to significant progresses published in a compendium of papers (Jordan, 1998). Since the ARI, further advances have been made by an array of programs; however, sea ice remote sensing signatures remain to be understood and further advanced. To model microwave radar signatures of snow-covered sea ice, the classical radiative transfer theory (RT; Tsang et al., 1985) accounts for incoherent intensity, but it does not truly preserve the phase information and does not satisfy Maxwell's equations. Then, the modified RT (MRT) was developed to keep the ladder terms in the Feynman diagrams (Mudaliar & Lee, 1993); however, MRT becomes extremely complex to include realistic characteristics of snow-covered sea ice. To overcome these limitations, Maxwell's equations are used to develop an advanced radar scattering theory in order to correctly capture and preserve both amplitude and phase information, which is imperative for measuring sea ice DEM. While numerical methods can solve Maxwell's equations (Nghiem et al., 2019; Tan et al., 2017) requiring a high computation demand that limits the realization of a realistic characterization of snow-covered sea ice, the analytic approach allows complex properties and processes of snow and ice to be accounted for Nghiem et al. (1990, 1995a, 1995b).

Over past decades, the analytic solution was successful in capturing: polarimetric backscatter signatures of sea ice verified with observations from the Beaufort Sea Field Campaign (Nghiem et al., 1995a, 1995b), effects on polarimetric backscatter from frost flowers on sea ice verified with data from the Cold Regions Research and Engineering Laboratory Experiment (CRRELEX; Nghiem et al., 1995), radar backscatter response to thin sea ice growth process measured during CRRELEX (Nghiem et al., 1997), role of snow on the thermal dependence of radar backscatter over sea ice observed during the Seasonal Sea Ice Monitoring and Modeling Site experiment (Barber & Nghiem, 1999), synthetic aperture radar (SAR) signatures of Arctic sea ice tested with measurements from the Jet Propulsion Laboratory Airborne SAR campaign (Nghiem & Bertoia, 2001), preparation for the operational use of RADARSAT-2 for ice monitoring (Ramsay et al., 2004), radiometric signatures of river ice status and river discharge verified with in situ data (Brakenridge et al., 2017), and backscatter signature of snowmelt on the Greenland ice sheet for snowmelt mapping validated with data from the Greenland Climate Network (Nghiem et al., 2001).

With the above background on the development and verification of the analytic method from past research experiences, we establish and present in this section the fundamental foundation for advanced radar polarimetric and interferometric measurements in order to guide the algorithm development for retrieval of sea ice DEM from satellite data acquired by SAR with polarimetric and interferometric capabilities such as TerraSAR-X (TSX) and TanDEM-X (TDX; Krieger et al., 2007). First, radar scattering coefficients are obtained with polarimetric and interferometric modeling based on the first principle of Maxwell's equations. Then, systematically informed by the symmetry group theory (Hamermesh, 1972), specific terms among the various complex polarimetric interferometric scattering coefficients in the covariance matrix are effectively selected to examine how radar measurements can be utilized to observe sea ice DEM.

2.1. Principle of Radar Polarimetric Inteferometry

For polarimetric interferometry, the deployment for radar measurements are illustrated in Figure 1. Consider a radar transmitting an incidence electric field $\overline{E}_{0i}$ toward a targeted area A on snow-covered sea ice, from which a scattered field $\overline{E}_{0s}\left(\overline{r}_a\right)$ is measured by a radar receiver at location $\overline{r}_a$ and another scattered field $\overline{E}_{0s}\left(\overline{r}_b\right)$ is measured by a different radar receiver at location $\overline{r}_b$. This radar measurement deployment allows observations of: (a) monostatic scattering by taking ensemble averages for scattered field correlations at $\overline{r}_a$, (b) bistatic scattering by taking ensemble averages for scattered field correlations at $\overline{r}_b$, and (c) interferometric scattering by taking cross-ensemble averages for scattered field correlations at the two locations $\overline{r}_a$ and $\overline{r}_b$.

The polarimetric interferometry theory in this paper will unify the treatment of all monostatic, bistatic, polarimetric, and interferometric radar deployment in a single formulation, where multifold integrations over complex

10.1029/2021EA002191

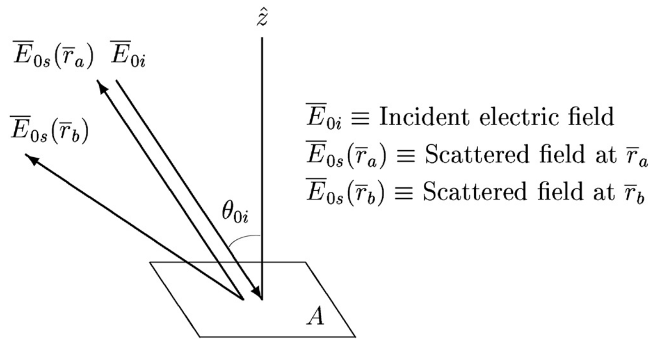

Figure 1. The bistatic fully polarimetric interferometric deployment.

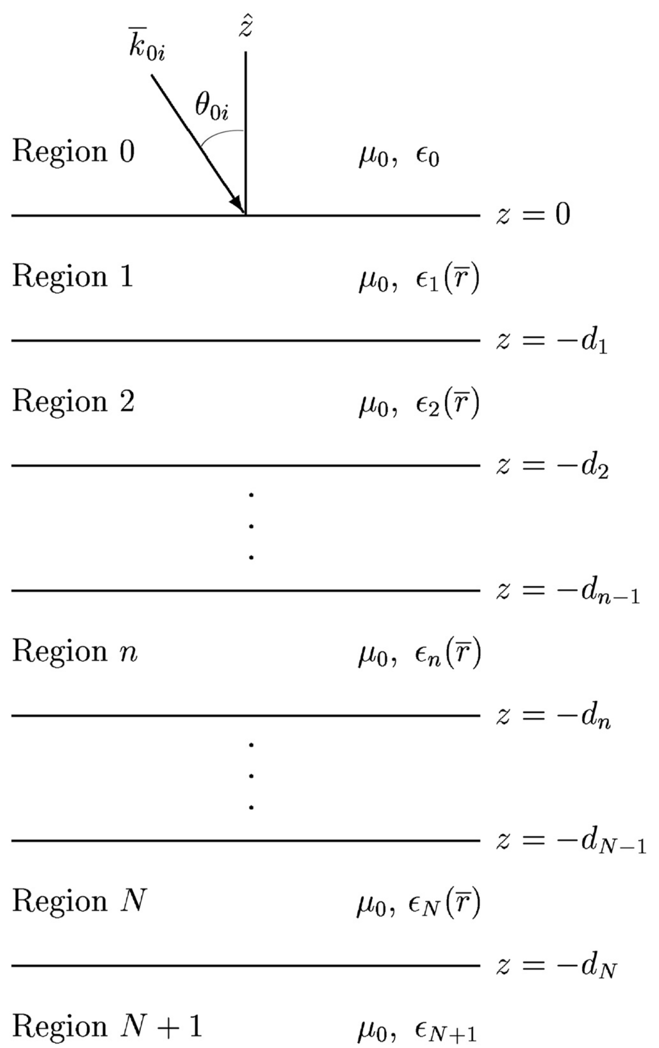

Figure 2. Multi-layered configuration of snow-covered sea ice.

variables for polarimetric backscatter, bistatic, and interferometric scattering coefficients are carried out over spatial and spectral domains for all propagation mechanisms of ordinary and extraordinary electromagnetic waves in multi-layered anisotropic media. Thereby, the unified theory intrinsically accounts for the interferometric phase, radar resolution cell, baseline decorrelation, rotation decorrelation, polarization diversity, depolarization effects, and characteristics of geophysical media.

2.2. Electromagnetic Modeling

2.2.1. Overall Formulation Concept

Electromagnetic modeling of geophysical media, such as snow-covered sea ice, based on the first principle of Maxwell's equations preserves the coherent phase information (Nghiem et al., 1990), which is fundamentally required for radar polarimetry and interferometry. Analytic solutions of Maxwell's equations that are computationally effective allow electromagnetic modeling of realistic and complicated properties of snow, sea ice, and seawater under various environmental conditions, and thereby providing insights into the scattering mechanisms and how they are related to physical characteristics of the geophysical media.

Within the concept of the analytic method, vector wave equations derived from Maxwell's equations are solved with dyadic Green's functions (DGFs) for a multi-layered configuration of snow-covered sea ice on seawater. Integral equations are cast from the vector wave equations to obtain electromagnetic fields under the distorted Born approximation subject to boundary conditions at the air-snow, snow-ice, and ice-seawater interfaces. DGFs account for multiple wave-boundary interactions including multiple transmissions, refractions, reflections, and differential phase and attenuation of ordinary and extraordinary waves propagating downward and upward in the anisotropic layered media. The influence of medium inhomogeneities on wave phase and attenuation is treated with a decomposition of DGFs into principal-value parts and Dirac-delta parts together with the renormalization method in the strong fluctuation theory based on bilocal-approximation solutions of Dyson's equations derived with the Feynman's diagram. Complex integrations are carried out with appropriate branch cuts and Riemann sheets.

The analytic modeling accounts for crystallographic structure of sea ice, uses realistic statistics of orientation and size distributions in snow and sea ice, and includes all wave-interaction types in the complex domain for all phases and polarization states of scattering signatures of snow-covered sea ice. Both absorption and scattering loss for wave propagation with multiple scattering effects are included in the calculation of effective permittivities to be valid beyond the quasi-static limit. For rough surface scattering at interfaces in the layered media, the model includes roughnesses with different scales represented by a probability function. Effects of salinity in effective dispersion relations of electromagnetic waves are also considered.

2.2.2. Multi-Layered Configuration

Stratified geophysical media, such as snow-covered sea ice on seawater, with variations in the vertical profile of their properties, are modeled with the multi-layered configuration in Figure 2. The upper half space represents the

10.1029/2021EA002191

air or free space where a remote-sensing radar is located to make measurements. Each layer between two interfaces is inhomogeneous with randomly embedded scatterers. The underlying medium is a homogeneous half space (e.g., seawater in polar oceans). The upper half space, labeled as region 0, has permittivity ϵ_0. At a depth of d_{n-1} (for $n = 1, 2, \ldots, n, \ldots, N + 1$), the interface between region $(n - 1)$ and region n is defined as the $(n - 1)$th planar interface (extension to rough surface will be included in another section below). The top interface or 0th interface is at location $z = -d_0 = 0$, and the bottom one or the Nth interface is at $z = -d_N$ in the Cartesian system $(\hat{x}, \hat{y}, \hat{z})$ where the hat denotes a unit vector.

Region n is characterized with inhomogeneous permittivity $\epsilon_n(\overline{r})$, which takes on value ϵ_{bn} if location $\overline{r}$ is in the background medium indicated by subscript b, and the value is ϵ_{sn} in scatterers represented by subscript s. For $\overline{r}$ and other quantities in this paper, the single overbar indicates a vector. The underlying half space is region $N + 1$ with homogeneous permittivity ϵ_{N+1}. Dependent on a preferential alignment of scatterers, a medium in the multi-layered configuration can be effectively anisotropic with a tilted optic axis. All media are non-magnetic with permeability denoted by μ_0.

2.2.3. Governing Equations

Derived from Maxwell's equations, the time-harmonic total fields $\overline{E}_0(\overline{r})$, $\overline{E}_n(\overline{r})$, and $\overline{E}_{N+1}(\overline{r})$ in regions 0, n, and $N + 1$ are governed by the following vector wave equations in the phasor form:

$$\nabla \times \nabla \times \overline{E}_0(\overline{r}) - k_0^2 \overline{E}_0(\overline{r}) = 0 \tag{1}$$

$$\nabla \times \nabla \times \overline{E}_n(\overline{r}) - k_0^2 \frac{\epsilon_n(\overline{r})}{\epsilon_0} \overline{E}_n(\overline{r}) = 0 \tag{2}$$

$$\nabla \times \nabla \times \overline{E}_{N+1}(\overline{r}) - k_0^2 \frac{\epsilon_{N+1}}{\epsilon_0} \overline{E}_{N+1}(\overline{r}) = 0 \tag{3}$$

where the free-space wave number is $k_0 = \omega\sqrt{\mu_0 \epsilon_0}$ and the angular frequency is $\omega = 2\pi f$ for wave frequency f.

In snow-covered sea ice, differences in permittivities of materials in a heterogeneous layer are encountered (e.g., ice grains in snow, and air bubbles or brine inclusions in sea ice). To account for the permittivity fluctuations, the medium in region n is represented with an auxiliary anisotropic permittivity tensor $\overline{\overline{\epsilon}}_{gn}$ (the double over bars denote a tensor). Introducing $\overline{\overline{\epsilon}}_{gn}$ in both sides of Equation 2, the wave equation becomes:

$$\nabla \times \nabla \times \overline{E}_n(\overline{r}) - k_0^2 \frac{\overline{\overline{\epsilon}}_{gn}}{\epsilon_0} \cdot \overline{E}_n(\overline{r}) = k_0^2 \overline{\overline{Q}}_n(\overline{r}) \cdot \overline{E}_n(\overline{r}) \tag{4}$$

where the source term on the right-hand side of Equation 4 is related to the tensor difference between $\epsilon_n(\overline{r})\overline{\overline{I}}$ and $\overline{\overline{\epsilon}}_{gn}$ as follows:

$$k_0^2 \overline{\overline{Q}}_n(\overline{r}) \cdot \overline{E}_n(\overline{r}) = k_0^2 \left[\frac{\epsilon_n(\overline{r})\overline{\overline{I}} - \overline{\overline{\epsilon}}_{gn}}{\epsilon_0} \right] \cdot \overline{E}_n(\overline{r}) \tag{5}$$

in which $\overline{\overline{I}}$ is the unit dyad. The determination of $\overline{\overline{\epsilon}}_{gn}$ will be presented later in the framework of the strong fluctuation theory. Physically, $\overline{\overline{\epsilon}}_{gn}$ is the effective permittivity tensor in the very low frequency limit and $\overline{\overline{\epsilon}}_{gn}$ characterizes wave propagation and attenuation in an effective medium without scattering effects. The dispersive scattering effects will be included in a frequency-dependent permittivity term to be presented later.

In the integral equation form, the total field in region $m = 0, 1, 2, \ldots, N, N + 1$ is a superposition of the mean field and the scattered field:

$$\overline{E}_m(\overline{r}) = \overline{E}_m^{(0)}(\overline{r}) + k_0^2 \sum_{n=1}^{N} \int_{V_n} d\overline{r}_n \overline{\overline{G}}_{mn}(\overline{r}, \overline{r}_n) \cdot \overline{\overline{Q}}_n(\overline{r}_n) \cdot \overline{E}_n(\overline{r}_n) \tag{6}$$

10.1029/2021EA002191

where V_n is the space occupied by region n and mean field $\overline{E}^{(0)}_m(\overline{r})$ is the solution to the wave equations where the scattering sources vanish. The second term in Equation 6 is the scattered field, which involves DGF $\overline{\overline{G}}_{mn}(\overline{r},\overline{r}_n)$ determined by:

$$\nabla \times \nabla \times \overline{\overline{G}}_{mn}(\overline{r},\overline{r}_n) - k_0^2 \frac{\overline{\overline{\epsilon}}_{gm}}{\epsilon_0} \cdot \overline{\overline{G}}_{mn}(\overline{r},\overline{r}_n) = \delta(\overline{r}-\overline{r}_n)\,\overline{\overline{I}} \tag{7}$$

where subscript m in $\overline{\overline{G}}_{mn}(\overline{r},\overline{r}_n)$ denotes the observation region containing observation point $\overline{r}$, subscript n represents source region $n = 1, 2, \ldots, N$ containing source point $\overline{r}_n$, and $\delta(\overline{r}-\overline{r}_n)$ is the Dirac delta function. When $m \neq n$, observation point $\overline{r}$ is outside source region n where $\overline{r}_n$ is confined, the Dirac delta function in the right-hand side of Equation 7 vanishes. Within a scattering region, an observation point can coincide with a source point in the same region ($m = n = 1, 2, \ldots, N$) causing the singularity in the DGF. In this case, $\overline{\overline{G}}_{nn}(\overline{r},\overline{r}_n)$ is decomposed into a principal value part and a Dirac delta part:

$$\overline{\overline{G}}_{nn}(\overline{r},\overline{r}_n) = PV\overline{\overline{G}}_{nn}(\overline{r},\overline{r}_n) - \delta(\overline{r}-\overline{r}_n)\,k_0^{-2}\overline{\overline{S}}_n \tag{8}$$

where dyadic coefficient $\overline{\overline{S}}_n$ conforms with the shape of the source exclusion volume. With this decomposition, the singular part in the integrand on the right-hand side of Equation 6 for $m = n$ is extracted and then combined with total field $\overline{E}_n(\overline{r})$ on the left-hand side to form external field $\overline{F}_n(\overline{r})$:

$$\overline{F}_n(\overline{r}) = \left[\overline{\overline{I}} + \overline{\overline{S}}_n \cdot \overline{\overline{Q}}_n(\overline{r})\right] \cdot \overline{E}_n(\overline{r}) \tag{9}$$

In terms of external field $\overline{F}_n(\overline{r})$, the vector source in Equation 5 is redefined by introducing scatterer $\overline{\overline{\xi}}_n(\overline{r})$ such that:

$$k_0^2\overline{\overline{\xi}}_n(\overline{r}) \cdot \overline{F}_n(\overline{r}) = k_0^2\overline{\overline{Q}}_n(\overline{r}) \cdot \overline{E}_n(\overline{r}) \tag{10}$$

It follows from Equation 10 that scatterer $\overline{\overline{\xi}}_n(\overline{r})$ region n is:

$$\overline{\overline{\xi}}_n(\overline{r}) = \overline{\overline{Q}}_n(\overline{r}) \cdot \left[\overline{\overline{I}} + \overline{\overline{S}}_n \cdot \overline{\overline{Q}}_n(\overline{r})\right]^{-1} \tag{11}$$

By applying the distorted Born approximation to Equation 8 with the new definition of the sources by Equation 6, the total field observed in region 0 is:

$$\overline{E}_0(\overline{r}) = \overline{E}^{(0)}_0(\overline{r}) + k_0^2 \sum_{n=1}^{N} \int_{V_n} d\overline{r}_n\, \overline{\overline{G}}^{(0)}_{0n}(\overline{r},\overline{r}_n) \cdot \overline{\overline{\xi}}_n(\overline{r}_n) \cdot \overline{F}^{(0)}_n(\overline{r}_n) \tag{12}$$

where effective permittivity tensor $\overline{\overline{\epsilon}}_{effn}$ is used to calculate mean DGF $\overline{\overline{G}}^{(0)}_{0n}(\overline{r},\overline{r}_n)$ and mean field $\overline{F}^{(0)}_n(\overline{r}_n)$.

Here, the wave propagation and attenuation are characterized by complex effective permittivity. The mixing of scatterers (e.g., ice grains in snow, air bubbles and brine inclusions in sea ice, etc.) in a host medium determines an effective permittivity tensor that governs wave propagation and attenuation in the inhomogeneous medium. The dispersion of the medium not only depends on dispersive permittivities of the constituents but also on scattering effects of the inhomogeneities. The strong permittivity fluctuation theory (Tsang et al., 1985) is used to derive the effective permittivity tensor. The singularity of the DGF is accounted for and the derivation is carried out in the frequency domain. The theory is based on bilocal-approximation solutions of Dyson's equations derived with the Feynman's diagram, where complex integrations are carried out with appropriate considerations of branch cuts and Riemann sheets in the complex plane of transcendental functions. Specific mathematical expression for complex effective permittivity can be obtained following the method of Nghiem et al. (1996), including thermodynamic effects in sea ice.

2.2.4. Scattered Field Ensembles

A radar can measure both magnitudes and phases of scattered fields at two different locations $\bar{r}_a$ and $\bar{r}_b$. The scattered fields are correlated to form backscatter images, bistatic images, interferometric correlation maps, or interferograms. Ensembles averages of scattered field products, also called scattered field correlations, are obtained from Equation 12 as:

$$\langle \overline{E}_{0s}(\bar{r}_a) \cdot \overline{E}^*_{0s}(\bar{r}_b) \rangle = \sum_{n=1}^{N} \sum_{i,j,k,l,m}^{x,y,z} k_0^4 \int_{V_n} d\bar{r}_n \int_{V_n} d\bar{r}^o_n \, C_{\xi njklm}(\bar{r}_n, \bar{r}^o_n) \cdot \left[G^{(0)}_{0nij}(\bar{r}_a, \bar{r}_n) \, F^{(0)}_{nk}(\bar{r}_n) \right] \cdot \left[G^{(0)}_{0nil}(\bar{r}_b, \bar{r}^o_n) \, F^{(0)}_{nm}(\bar{r}^o_n) \right]^* \tag{13}$$

where subscripts a and b are for the receiver locations, and $C_{\xi njklm}(\bar{r}_n, \bar{r}^o_n)$ is the $jklm$ element of the fourth-rank correlation tensor $\overline{\overline{C}}_{\xi n}(\bar{r}_n, \bar{r}^o_n)$ for scatterers in region n and is:

$$C_{\xi njklm}(\bar{r}_n, \bar{r}^o_n) = \left\langle \xi_{njk}(\bar{r}_n) \, \xi^*_{nlm}(\bar{r}^o_n) \right\rangle = \int_{-\infty}^{\infty} d\bar{\beta} \, C_{\xi njklm}(\bar{\beta}) \, e^{-i\bar{\beta}\cdot(\bar{r}_n - \bar{r}^o_n)} \tag{14}$$

in which the spectral density is $C_{\xi njklm}(\bar{\beta}) = \Gamma^{(C)}_{\xi njklm} \Phi_{\xi n}(\bar{\beta})$ with variance $\Gamma^{(C)}_{\xi njklm}$. Note that $\Phi_{\xi n}(\bar{\beta})$ is the same as that used to calculate effective permittivities. The scatterers are consistently described in the calculations of wave scattering, propagation, and attenuation. In Equation 13, elements in the mean DGF $\overline{\overline{G}}^{(0)}_{0n}(\bar{r}, \bar{r}_n)$ for $\bar{r} = \bar{r}_a, \bar{r}_b$ and in the external field $\overline{F}^{(0)}_n(\bar{r}_n)$ are necessary to obtain the scattered field correlations.

2.2.5. Dyadic Green's Function

DGF $\overline{\overline{G}}^{(0)}_{0n}(\bar{r}, \bar{r}_s)$ for observation point $\bar{r}$ in region 0 and source point $\bar{r}_s$ in region n is derived from $\overline{\overline{G}}^{(0)}_{n0}(\bar{r}_s, \bar{r})$ for the source in region 0 and the observation in region n with the symmetric relation (Tai, 1971):

$$\overline{\overline{G}}^{(0)}_{mn}(\bar{r}, \bar{r}_s) = \overline{\overline{G}}^{(0)\top}_{nm}(\bar{r}_s, \bar{r}) \tag{15}$$

The DGFs for regions 0, $n = 0, 1, 2, \ldots, N, N+1$ are determined by dyadic wave equations:

$$\nabla \times \nabla \times \overline{\overline{G}}^{(0)}_{00}(\bar{r}, \bar{r}_s) - k_0^2 \cdot \overline{\overline{G}}^{(0)}_{00}(\bar{r}, \bar{r}_s) = \delta(\bar{r} - \bar{r}_s)\,\overline{\overline{I}}, z \geq 0 \tag{16}$$

$$\nabla \times \nabla \times \overline{\overline{G}}^{(0)}_{n0}(\bar{r}, \bar{r}_s) - k_0^2 \frac{\overline{\overline{\epsilon}}_{effn}}{\epsilon_0} \cdot \overline{\overline{G}}^{(0)}_{n0}(\bar{r}, \bar{r}_s) = 0, -d_{n-1} \geq z \geq -d_n \tag{17}$$

$$\nabla \times \nabla \times \overline{\overline{G}}^{(0)}_{(N+1)0}(\bar{r}, \bar{r}_s) - k_0^2 \frac{\epsilon_{N+1}}{\epsilon_0} \cdot \overline{\overline{G}}^{(0)}_{(N+1)0}(\bar{r}, \bar{r}_s) = 0, -d_N \geq z \tag{18}$$

The DGFs are subject to the radiation condition at infinite distances above and below the interfaces. At the interfaces (e.g., air-snow, snow-ice, ice-seawater), DGFs have to satisfy boundary conditions requiring the continuity of $\hat{z} \times \overline{\overline{G}}^{(0)}_{n0}$ and $\hat{z} \times \nabla \times \overline{\overline{G}}^{(0)}_{n0}$ for the tangential electric and magnetic fields as:

$$\left.\begin{aligned} \hat{z} \times \overline{\overline{G}}^{(0)}_{00}(\bar{r}, \bar{r}_s) &= \hat{z} \times \overline{\overline{G}}^{(0)}_{10}(\bar{r}, \bar{r}_s) \\ \hat{z} \times \nabla \times \overline{\overline{G}}^{(0)}_{00}(\bar{r}, \bar{r}_s) &= \hat{z} \times \nabla \times \overline{\overline{G}}^{(0)}_{10}(\bar{r}, \bar{r}_s) \end{aligned}\right\} \text{ at } z = 0 \tag{19}$$

$$\left.\begin{aligned} \hat{z} \times \overline{\overline{G}}^{(0)}_{n0}(\bar{r}, \bar{r}_s) &= \hat{z} \times \overline{\overline{G}}^{(0)}_{(n+1)0}(\bar{r}, \bar{r}_s) \\ \hat{z} \times \nabla \times \overline{\overline{G}}^{(0)}_{n0}(\bar{r}, \bar{r}_s) &= \hat{z} \times \nabla \times \overline{\overline{G}}^{(0)}_{(n+1)0}(\bar{r}, \bar{r}_s) \end{aligned}\right\} \text{ at } z = -d_n \tag{20}$$

$$\left.\begin{aligned}\hat{z}\times\overline{\overline{G}}^{(0)}_{N0}\left(\overline{r},\overline{r}_s\right) &= \hat{z}\times\overline{\overline{G}}^{(0)}_{(N+1)0}\left(\overline{r},\overline{r}_s\right)\\ \hat{z}\times\nabla\times\overline{\overline{G}}^{(0)}_{N0}\left(\overline{r},\overline{r}_s\right) &= \hat{z}\times\nabla\times\overline{\overline{G}}^{(0)}_{(N+1)0}\left(\overline{r},\overline{r}_s\right)\end{aligned}\right\}\text{ at } z=-d_N \tag{21}$$

With the saddle point method, the solution for DGF $\overline{\overline{G}}^{(0)}_{0n}\left(\overline{r},\overline{r}_s\right)$ in the radiation field can be written in the following form (Lee & Kong, 1985):

$$\overline{\overline{G}}^{(0)}_{0n}\left(\overline{r},\overline{r}_s\right) = \frac{e^{ik_0 r}}{4\pi r}\, e^{-i\overline{k}_\rho\cdot\overline{\rho}_s}\,\overline{\overline{g}}_n\left(\overline{k}_\rho, k^w_{nz}, z_s\right) \tag{22}$$

where $\overline{k}_\rho$ is the lateral wave vector, k^w_{nz} is the vertical component of the wave vector for wave type w, and $\overline{\rho}_s = \hat{x}x_s + \hat{y}y_s$. Representing multiple wave interactions with medium boundaries in layered media, dyadic coefficient $\overline{\overline{g}}_n\left(\overline{k}_\rho, k^w_{nz}, z_s\right)$ is defined as:

$$\begin{aligned}\overline{\overline{g}}_n\left(\overline{k}_\rho, k^w_{nz}, z_s\right) = \sum_\mu\sum_\nu \hat{\mu}\left(k^u_{0z}\right)\Big[&D_{n\mu\nu}\left(-\overline{k}_\rho\right)\hat{\nu}\left(k^{\nu u}_{nz}\right)\\ &\times e^{-ik^{\nu u}_{nz}z_s} + U_{n\mu\nu}\left(-\overline{k}_\rho\right)\hat{\nu}\left(k^{\nu d}_{nz}\right)e^{-ik^{\nu d}_{nz}z_s}\Big]\end{aligned} \tag{23}$$

where $\mu = h, v$ is for horizontal h or vertical v polarization, and u and d for upgoing and downgoing directions, respectively. If region n is isotropic, the characteristic wave has horizontal h or vertical v polarization, ν is h or v, and the wave types are $w = hu, hd, vu, vd$. Also, there is no distinction in the propagation of horizontal or vertical wave; therefore, $k^{hu}_{nz} = k^{vu}_{nz} \equiv k^u_{nz}$ and $k^{hd}_{nz} = k^{vd}_{nz} \equiv k^d_{nz}$. If region n is anisotropic, the characteristic waves are ordinary o or extraordinary e and $\nu = o, e$. In this case, there are four wave types $w = ou, od, eu, ed$ for ordinary upgoing, ordinary downgoing, extraordinary upgoing, and extraordinary downgoing waves. These account for the anisotropic wave speed difference and differential attenuation.

2.2.6. External Fields

External field $\overline{F}^{(0)}_n\left(\overline{r}\right)$ in region n are obtained from solutions of vector wave equations:

$$\nabla\times\nabla\times\overline{F}^{(0)}_n\left(\overline{r}\right) - k_0^2\frac{\overline{\overline{\epsilon}}_{eff\,n}}{\epsilon_0}\overline{F}^{(0)}_n\left(\overline{r}\right) = 0,\quad n = 1, 2, \ldots, N \tag{24}$$

which are solved subject to the boundary conditions at interface $z = 0, -d_1, -d_2, \ldots, d_N$. For incidence field $\overline{E}_{0i} = \left[\hat{h}\left(k_{0zi}\right)E_{hi} + \hat{v}\left(k_{0zi}\right)E_{vi}\right]e^{i\overline{k}_{0i}\cdot\overline{r}}$ propagating in the direction of incidence wave vector $\overline{k}_{0i}$ whose z component is k_{0zi}, the mean fields is:

$$\overline{F}^{(0)}_n\left(\overline{r}\right) = e^{\overline{k}_{\rho i}\cdot\overline{\rho}}\,\overline{P}_n\left(\overline{k}_{\rho i}, k^w_{nzi}, z\right),\quad n = 1, 2 \tag{25}$$

where subscript i indicates the incidence wave, $\overline{\rho} = \hat{x}x + \hat{y}y$ is the lateral spatial vector, $\overline{k}_{\rho i} = \hat{x}k_{xi} + \hat{y}k_{yi} = k_0\left(\hat{x}\sin\theta_{0i}\cos\phi_{0i} + \hat{y}\sin\theta_{0i}\sin\phi_{0i}\right)$ is the lateral incidence wave vector with incidence angle θ_{0i} and azimuthal angle ϕ_{0i}, and k^w_{nzi} is the vertical component of the wave vector for wave type w in region n.

Polarization vector $\overline{P}_n\left(\overline{k}_{\rho i}, k^w_{nzi}, z\right)$ in Equation 25 is expressed as follows:

$$\begin{aligned}\overline{P}_n\left(\overline{k}_{\rho i}, k^w_{nzi}, z\right) = \sum_\mu\sum_\nu E_{\mu i}\Big[&D_{n\mu\nu}\left(\overline{k}_{\rho i}\right)\hat{\nu}\left(k^{\nu d}_{nzi}\right)e^{ik^{\nu d}_{nzi}z}\\ &+ U_{n\mu\nu}\left(\overline{k}_{\rho i}\right)\hat{\nu}\left(k^{\nu u}_{nzi}\right)e^{ik^{\nu u}_{nzi}z}\Big]\end{aligned} \tag{26}$$

where $\mu = h, v$ and $\nu = h, v$ in an isotropic layer or $\nu = o, e$ in an anisotropic layer.

Coefficients U and D are derived from boundary conditions with the matrix method. To illustrate wave interaction processes described by U's and D's, consider amplitude vector $\overline{A}_n$ of upgoing waves and $\overline{B}_n$ of downgoing

10.1029/2021EA002191

waves in region n. Amplitude vectors of waves, propagating away and toward each interface, are related with matrix equations:

$$\begin{bmatrix} \overline{A}_n \\ \overline{B}_{(n+1)} \end{bmatrix} = \begin{bmatrix} \overline{\overline{R}}_{n(n+1)} & \overline{\overline{T}}_{(n+1)n} \\ \overline{\overline{T}}_{n(n+1)} & \overline{\overline{R}}_{(n+1)n} \end{bmatrix} \cdot \begin{bmatrix} \overline{B}_n \\ \overline{A}_{(n+1)} \end{bmatrix} \tag{27}$$

In the upper half space (region 0), $\overline{B}_0$ is the amplitude vector of the incidence wave. In the underlying medium (region $N+1$) such as seawater beneath the sea ice layer, there is no upgoing wave and $\overline{\overline{R}}_{(N+1)N}$ and $\overline{\overline{T}}_{(N+1)N}$ are not needed. Amplitude vectors in different layers are related to incidence vector $\overline{B}_0$ by:

$$\overline{A}_n = \overline{\overline{U}}_n \cdot \overline{B}_0 \quad \text{and} \quad \overline{B}_n = \overline{\overline{D}}_n \cdot \overline{B}_0 \tag{28}$$

Elements in $\overline{\overline{U}}_n$ are $U_{n\mu\nu}$ and in $\overline{\overline{D}}_n$ are $D_{n\mu\nu}$. Matrix $\overline{\overline{U}}_0$ is defined as the reflection matrix $\overline{\overline{R}}_0$ for region 0 and $\overline{\overline{D}}_{N+1}$ is the transmission matrix $\overline{\overline{T}}_{N+1}$ for region $N+1$. From the system of matrix equations in Equation 27, downgoing and upgoing amplitude vectors are solved in terms of $\overline{B}_0$ and the results are then compared to Equation 28 to obtain coefficient matrices in the DGFs and the polarization vectors.

2.2.7. Integration Method

The correlation of the μ-polarized scattered field $E_{\mu s}\left(\overline{r}_a\right)$, received at $\overline{r}_a$ and excited by a τ-polarized incidence field $E_{\tau i}$, with the conjugated ν-polarized scattered field $E^*_{\nu s}\left(\overline{r}_b\right)$, received at $\overline{r}_b$ and excited by a conjugated κ-polarized incidence field $E^*_{\kappa i}$, is obtained from Equations 13, 14, 22, and 25 and expressed as:

$$\begin{aligned} \left\langle E_{\mu s}\left(\overline{r}_a\right) E^*_{\nu s}\left(\overline{r}_b\right)\right\rangle = E_{\tau i} E^*_{\kappa i} & \frac{k_0^4 e^{ik_0\left(r_a - r_b\right)}}{16\pi^2 r_a r_b} \sum_{n=1}^{N} \sum_{p,q,r,s}^{w} \sum_{j,k,l,m}^{x,y,z} \\ & \int_{-\infty}^{\infty} d\overline{\beta}_\rho \int_A d\overline{\rho}_n \int_A d\overline{\rho}_n^o \cdot e^{i\left(\overline{k}_{\rho i} - \overline{k}_\rho^a - \overline{\beta}_\rho\right)\cdot\overline{\rho}_n} e^{-i\left(\overline{k}_{\rho i} - \overline{k}_\rho^b - \overline{\beta}_\rho\right)\cdot\overline{\rho}_n^o} \\ & \int_{-\infty}^{\infty} d\beta_z \int_{-d_n}^{-d_{n-1}} dz_n \int_{-d_n}^{-d_{n-1}} dz_n^o \cdot e^{-i\beta_z\left(z_n - z_n^o\right)}\, C_{\xi njklm}\left(\overline{\beta}_\rho, \beta_z\right) \\ & \cdot g_{n\mu j}\left(\overline{k}_\rho^a, k_{nz}^{ap}, z_n\right)\, \mathcal{F}_{n\tau k}\left(\overline{k}_{\rho i}, k_{nzi}^q, z_n\right) \\ & \cdot g^*_{n\nu l}\left(\overline{k}_\rho^b, k_{nz}^{br}, z_n^o\right)\, \mathcal{F}^*_{n\kappa m}\left(\overline{k}_{\rho i}, k_{nzi}^s, z_n^o\right) \end{aligned} \tag{29}$$

where $\overline{\beta} = \overline{\beta}_\rho + \hat{z}\beta_z$, $\overline{\beta}_\rho = \hat{x}\beta_x + \hat{y}\beta_y$, subscripts $\mu, \nu, \tau, \kappa = h, v$, superscripts a and b indicate the receiver toward which the scattered waves propagate, subscripts p, q, r, s are for all wave types $w = hu, hd, vu, vd$ in an isotropic medium or $w = ou, od, eu, ed$ in an anisotropic medium, and the footprint A is the radar resolution cell. The bistatic fully polarimetric interferometric deployment depicted in Figure 1 has been used to arrive at Equation 29 where the incidence or excitation fields propagate in the same direction. DGF element $g_{n\mu j}\left(\overline{k}_\rho^a, k_{nz}^{ap}, z_n\right)$ and normalized mean field component $\mathcal{F}_{n\tau k}\left(\overline{k}_{\rho i}, k_{nzi}^q, z_n\right)$ for $\hat{j}, \hat{k} = \hat{x}, \hat{y}, \hat{z}$ are defined as:

$$g_{n\mu j}\left(\overline{k}_\rho^a, k_{nz}^{ap}, z_n\right) = \left[\hat{\mu}\left(k_{0z}^u\right) \cdot \overline{\overline{g}}_n\left(\overline{k}_\rho^a, k_{nz}^{ap}, z_n\right)\right] \cdot \hat{j} \tag{30}$$

$$\mathcal{F}_{n\tau k}\left(\overline{k}_{\rho i}, k_{nzi}^q, z_n\right) = E_{\tau i}^{-1} \overline{P}_n\left(\overline{k}_{\rho i}, k_{nzi}^q, z_n\right) \cdot \hat{k}\ \big|_{E_{\nu i}=0, \nu\neq\tau} \tag{31}$$

The scattered field correlation given by Equation 29 involves nine-fold integrations (2 for $d\overline{\beta}_\rho$, 2 for $d\overline{\rho}_n$, 2 for $d\overline{\rho}_n^o$, 1 for $d\beta_z$, 1 for $d\zeta_n$, and 1 for $d\zeta_n^o$). A methodology to carry out the integrations needs to be implemented. First, the integrands in Equation 29 are oscillatory due to the wave phases involving the lateral spaces. A spatial transformation is necessary such that the phases arrange themselves into a highly oscillatory term and a smooth term. Such a transformation is the following linear orthogonal mapping from $\overline{\rho}_n$ and $\overline{\rho}_n^o$ spaces to $\overline{R}_n$ and $\overline{R}_n^o$ spaces:

$$\overline{\rho}_n = \overline{R}_n + \overline{R}_n^o \quad \text{and} \quad \overline{\rho}_n^o = \overline{R}_n - \overline{R}_n^o \tag{32}$$

10.1029/2021EA002191

With the corresponding Jacobian $\partial\left(\overline{\rho}_n,\overline{\rho}_n^o\right)/\partial\left(\overline{R}_n,\overline{R}_n^o\right)$, substituting Equation 32 in Equation 29 renders:

$$\begin{aligned}\left\langle E_{\mu s}\left(\overline{r}_a\right)E_{\nu s}^*\left(\overline{r}_b\right)\right\rangle = E_{\tau i}E_{\kappa i}^*\frac{k_0^4e^{ik_0\left(r_a-r_b\right)}}{16\pi^2r_ar_b}\sum_{n=1}^{N}\sum_{p,q,r,s}^{w}\sum_{j,k,l,m}^{x,y,z}\frac{\partial\left(\overline{\rho}_n,\overline{\rho}_n^o\right)}{\partial\left(\overline{R}_n,\overline{R}_n^o\right)}\\ \int_{-\infty}^{\infty}d\overline{\beta}_\rho\int_A d\overline{R}_ne^{i\left(\overline{k}_\rho^b-\overline{k}_\rho^a\right)\cdot\overline{R}_n}\int_A d\overline{R}_n^o\,e^{i\left[2\overline{k}_{\rho i}-\left(\overline{k}_\rho^a+\overline{k}_\rho^b\right)-2\overline{\beta}_\rho\right]\cdot\overline{R}_n^o}\\ \int_{-\infty}^{\infty}d\beta_z\int_{-d_n}^{-d_{n-1}}dz_n\int_{-d_n}^{-d_{n-1}}dz_n^o\cdot e^{-i\beta_z\left(z_n-z_n^o\right)}C_{\xi njklm}\left(\overline{\beta}_\rho,\beta_z\right)\\ \cdot g_{n\mu j}\left(\overline{k}_\rho^a,k_{nz}^{ap},z_n\right)\mathcal{F}_{n\tau k}\left(\overline{k}_{\rho i},k_{nzi}^q,z_n\right)\\ \cdot g_{n\nu l}^*\left(\overline{k}_\rho^b,k_{nz}^{br},z_n^o\right)\mathcal{F}_{n\kappa m}^*\left(\overline{k}_{\rho i},k_{nzi}^s,z_n^o\right)\end{aligned}\tag{33}$$

The integrand in the integration over $d\overline{R}_n^o$ is highly oscillatory over resolution A unless $2\overline{\beta}_\rho$ approaches $2\overline{k}_{\rho i}-\left(\overline{k}_\rho^a+\overline{k}_\rho^b\right)$. This integration together with the Jacobian result in the delta function $4\pi^2\delta\left[2\overline{k}_{\rho i}-\left(\overline{k}_\rho^a+\overline{k}_\rho^b\right)-2\overline{\beta}_\rho\right]$. Then, the delta function sets $\overline{\beta}_\rho=\overline{k}_{\rho i}-\left(\overline{k}_\rho^a+\overline{k}_\rho^b\right)/2$ by the sifting property for the integration over $d\overline{\beta}_\rho$. Now, five-fold integrations remain in:

$$\begin{aligned}\left\langle E_{\mu s}\left(\overline{r}_a\right)E_{\nu s}^*\left(\overline{r}_b\right)\right\rangle = E_{\tau i}E_{\kappa i}^*\frac{k_0^4e^{ik_0\left(r_a-r_b\right)}}{4r_ar_b}\sum_{n=1}^{N}\sum_{p,q,r,s}^{w}\sum_{j,k,l,m}^{x,y,z}\\ \int_A d\overline{R}_ne^{i\left(\overline{k}_\rho^b-\overline{k}_\rho^a\right)\cdot\overline{R}_n}\int_{-\infty}^{\infty}d\beta_z\int_{-d_n}^{-d_{n-1}}dz_n\int_{-d_n}^{-d_{n-1}}dz_n^o\cdot e^{-i\beta_z\left(z_n-z_n^o\right)}\\ C_{\xi njklm}\left(\overline{k}_{\rho i}-\frac{\overline{k}_\rho^a+\overline{k}_\rho^b}{2},\beta_z\right)\cdot g_{n\mu j}\left(\overline{k}_\rho^a,k_{nz}^{ap},z_n\right)\mathcal{F}_{n\tau k}\left(\overline{k}_{\rho i},k_{nzi}^q,z_n\right)\\ \cdot g_{n\nu l}^*\left(\overline{k}_\rho^b,k_{nz}^{br},z_n^o\right)\mathcal{F}_{n\kappa m}^*\left(\overline{k}_{\rho i},k_{nzi}^s,z_n^o\right)\end{aligned}\tag{34}$$

For azimuth resolution X and range resolution Y, $A=XY$. Also, let $\overline{k}_\rho^{ab}=\overline{k}_\rho^b-\overline{k}_\rho^a$ or equivalently $k_x^{ab}=k_x^b-k_x^a$ and $k_y^{ab}=k_y^b-k_y^a$. The integrations over $d\overline{R}_n$ in range and azimuth are readily carried out, with the sinc function $\mathrm{sinc}(x)=x^{-1}\sin(x)$, to obtain:

$$\begin{aligned}\left\langle E_{\mu s}\left(\overline{r}_a\right)E_{\nu s}^*\left(\overline{r}_b\right)\right\rangle = E_{\tau i}E_{\kappa i}^*\frac{k_0^4\ A\ e^{ik_0\left(r_a-r_b\right)}}{4r_ar_b}\ \mathrm{sinc}\left(\frac{k_x^{ab}X}{2}\right)\mathrm{sinc}\left(\frac{k_y^{ab}Y}{2}\right)\\ \sum_{n=1}^{N}\sum_{p,q,r,s}^{w}\sum_{j,k,l,m}^{x,y,z}\int_{-\infty}^{\infty}d\beta_z\int_{-d_n}^{-d_{n-1}}dz_n\int_{-d_n}^{-d_{n-1}}dz_n^oe^{-i\beta_z\left(z_n-z_n^o\right)}\\ \cdot C_{\xi njklm}\left(\overline{k}_{\rho i}-\frac{\overline{k}_\rho^a+\overline{k}_\rho^b}{2},\beta_z\right)\cdot g_{n\mu j}\left(\overline{k}_\rho^a,k_{nz}^{ap},z_n\right)\mathcal{F}_{n\tau k}\left(\overline{k}_{\rho i},k_{nzi}^q,z_n\right)\\ \cdot g_{n\nu l}^*\left(\overline{k}_\rho^b,k_{nz}^{br},z_n^o\right)\mathcal{F}_{n\kappa m}^*\left(\overline{k}_{\rho i},k_{nzi}^s,z_n^o\right)\end{aligned}\tag{35}$$

To simplify the form of Equation 35 for the remaining integrations, coefficients in g and $\mathcal{F}$ that are independent of β_z, z_n, and z_n^o are taken out of the integrands. For this purpose, we define the following relations:

$$\begin{aligned}g_{n\mu j}\left(\overline{k}_\rho^a,k_{nz}^{ap},z_n\right)&=g_{n\mu j}\left(\overline{k}_\rho^a,k_{nz}^{ap}\right)\ e^{-ik_{nz}^{ap}z_n}\\ \mathcal{F}_{n\tau k}\left(\overline{k}_{\rho i},k_{nzi}^q,z_n\right)&=\mathcal{F}_{n\tau k}\left(\overline{k}_{\rho i},k_{nzi}^q\right)\ e^{ik_{nzi}^qz_n}\\ g_{n\nu l}^*\left(\overline{k}_\rho^b,k_{nz}^{br},z_n^o\right)&=g_{n\nu l}^*\left(\overline{k}_\rho^b,k_{nz}^{br}\right)\ e^{ik_{nz}^{br*}z_n^o}\\ \mathcal{F}_{n\kappa m}^*\left(\overline{k}_{\rho i},k_{nzi}^s,z_n^o\right)&=\mathcal{F}_{n\kappa m}^*\left(\overline{k}_{\rho i},k_{nzi}^s\right)\ e^{-ik_{nzi}^{s*}z_n^o}\end{aligned}\tag{36}$$

$$\begin{aligned}\kappa_{npq}^a&=-k_{nz}^{ap}+k_{nzi}^q\ ;\ p,q\in\{hu,hd,vu,vd\},\{ou,od,eu,ed\}\\ \kappa_{nrs}^b&=-k_{nz}^{br*}+k_{nzi}^{s*}\ ;\ r,s\in\{hu,hd,vu,vd\},\{ou,od,eu,ed\}\end{aligned}\tag{37}$$

By combining wave numbers in the exponential functions in Equations 35 and 36 and using the definitions for wave numbers in Equation 37, the triple integrations over $d\beta_z$, dz_n, and dz_n^0 are:

$$\mathcal{I}_{n,jklm}^{ab,pqrs} = \int_{-\infty}^{\infty} d\beta_z \quad C_{\xi njklm}\left(\overline{k}_{\rho i} - \frac{\overline{k}_{\rho}^{a} + \overline{k}_{\rho}^{b}}{2}, \beta_z\right) \int_{-d_n}^{-d_{n-1}} dz_n e^{-i\left(\beta_z - \kappa_{npq}^{a}\right)z_n} \int_{-d_n}^{-d_{n-1}} dz_n^o e^{i\left(\beta_z - \kappa_{nrs}^{b}\right)z_n^o} \tag{38}$$

where the integrations over dz_n and dz_n^0 for the vertical spaces are readily obtained. The integrated results introduce simple poles determined by z components of wave vectors so that for all wave types in the complex β_z plane as seen in the following expression for $\mathcal{I}_{n,jklm}^{ab,pqrs}$:

$$\mathcal{I}_{n,jklm}^{ab,pqrs} = \int_{-\infty}^{\infty} d\beta_z \quad C_{\xi njklm}\left(\overline{k}_{\rho i} - \frac{\overline{k}_{\rho}^{a} + \overline{k}_{\rho}^{b}}{2}, \beta_z\right) \cdot \frac{e^{i\left(\beta_z - \kappa_{npq}^{a}\right)d_{n-1}} - e^{i\left(\beta_z - \kappa_{npq}^{a}\right)d_n}}{\beta_z - \kappa_{npq}^{a}} \cdot \frac{e^{-i\left(\beta_z - \kappa_{nrs}^{b}\right)d_{n-1}} - e^{-i\left(\beta_z - \kappa_{nrs}^{b}\right)d_n}}{\beta_z - \kappa_{nrs}^{b}} \tag{39}$$

The last integration over $d\beta_z$ depends on statistical descriptions of the inhomogeneous media by spectral density $C_{\xi njklm}$. For $C_{\xi njklm}$ containing high order poles in upper and lower half planes and vanishing at the infinite extent of the complex β_z-plane, the integration over $d\beta_z$ is carried out by closing appropriate integration contours. For poles in the upper half plane and the term in Equation 39 involving the exponential function $\exp\left[i\left(d_n - d_{n-1}\right)\beta_z\right]$, the contour integration is taken along the positive real axis and along the upper infinite semi-circle on the complex β_z-plane so that the integration is converged. Similarly for the lower poles and the term in Equation 39 involving $\exp\left[-i\left(d_n - d_{n-1}\right)\beta_z\right]$, the infinite semi-circle contour is in the lower β_z-plane. Thus we have:

$$\begin{aligned} &\mathcal{I}_{n,jklm}^{ab,pqrs+} = \rightarrow + \nearrow^{0} = 2\pi i\left(\mathrm{Res}^{+}\right) \\ \text{and}\quad &\mathcal{I}_{n,jklm}^{ab,pqrs-} = \rightarrow + \swarrow^{0} = -2\pi i\left(\mathrm{Res}^{-}\right) \end{aligned} \tag{40}$$

where arrows are for integrations along the real axis, $\nearrow^{0}$ is the integration along the upper semi-circle, and $\nearrow^{0}$ along the lower one. Note that the semi-circle integrations vanish due to Jordan's lemma. In Equation 40, the residue theorem is applied and Res^+ and Res^- are residues of the poles in the upper and lower halves of the β_z-plane. Then, from Equation 40, $\mathcal{I}_{n,jklm}^{ab,pqrs}$ becomes:

$$\mathcal{I}_{n,jklm}^{ab,pqrs} = \mathcal{I}_{n,jklm}^{ab,pqrs+} + \mathcal{I}_{n,jklm}^{ab,pqrs-} = 2\pi i\left(\mathrm{Res}^{+} - \mathrm{Res}^{-}\right) \tag{41}$$

Thus, all nine-fold integrations in Equation 29 can be carried out. From Equations 35–41, we obtain the scattered field ensemble:

$$\left\langle E_{\mu s}\left(\overline{r}_a\right) E_{\nu s}^{*}\left(\overline{r}_b\right)\right\rangle = E_{\tau i} E_{\kappa i}^{*} \frac{A\, e^{ik_0\left(r_a - r_b\right)}}{4\pi r_a r_b} \operatorname{sinc}\left(\frac{k_x^{ab} X}{2}\right) \operatorname{sinc}\left(\frac{k_y^{ab} Y}{2}\right) \sum_{n=1}^{N} \sum_{p,q,r,s}^{w} \sum_{j,k,l,m}^{x,y,z} \Psi_{n,\mu\tau,jk}^{a,pq}\, \Psi_{n,\nu\kappa,lm}^{b,rs*}\, \mathcal{I}_{n,jklm}^{ab,pqrs} \tag{42}$$

where we have defined the following quantities:

$$\begin{aligned} \Psi_{n,\mu\tau,jk}^{a,pq} &= \pi \frac{1}{2} k_0^2 \quad g_{n\mu j}\left(\overline{k}_{\rho}^{a}, k_{nz}^{ap}\right) \mathcal{F}_{n\tau k}\left(\overline{k}_{\rho i}, k_{nzi}^{q}\right) \\ \Psi_{n,\nu\kappa,lm}^{b,rs*} &= \pi \frac{1}{2} k_0^2 \quad g_{n\nu l}^{*}\left(\overline{k}_{\rho}^{b}, k_{nz}^{br}\right) \mathcal{F}_{n\kappa m}^{*}\left(\overline{k}_{\rho i}, k_{nzi}^{s}\right) \end{aligned} \tag{43}$$

2.2.8. Covariance Matrix for Polarimetric Interferometry

The covariance matrix for the generalized fully polarimetric interferometry is a complex matrix defined in the linear polarization basis as:

$$\overline{\overline{C}}_{\chi} = \begin{bmatrix} \chi_{hhhh} & \chi_{hhhv} & \chi_{hhvh} & \chi_{hhvv} \\ \chi_{hvhh} & \chi_{hvhv} & \chi_{hvvh} & \chi_{hvvv} \\ \chi_{vhhh} & \chi_{vhhv} & \chi_{vhvh} & \chi_{vhvv} \\ \chi_{vvhh} & \chi_{vvhv} & \chi_{vvvh} & \chi_{vvvv} \end{bmatrix} \tag{44}$$

in which the elements are given by the following relation:

$$\chi_{\mu\tau\nu\kappa} = 4\pi r_a r_b \langle E_{\mu s}\left(\overline{r}_a\right) \cdot E^*_{\nu s}\left(\overline{r}_b\right)\rangle / \left(A\ E_{\tau i} E^*_{\kappa i}\right) \tag{45}$$

where E is the electric field transmitted (denoted by subscript i) and received (denoted by subscript s) by the radar, subscripts $\mu, \nu, \tau, \kappa = h, v$, superscripts a and b indicate the receiver toward which the scattered waves propagate, and A is the radar resolution cell. The bistatic fully polarimetric interferometric deployment is depicted in Figure 1 where the incidence or excitation fields propagate in the same direction.

From Equations 42, 43, and 45 together with the resolution correlation coefficient given by the product $\rho_X \rho_Y$ for $\rho_X = \mathrm{sinc}\left(k_x^{ab} X/2\right)$ in azimuth and $\rho_Y = \mathrm{sinc}\left(k_y^{ab} Y/2\right)$ in range, polarimetric interferometry scattering coefficient $\chi_{\mu\tau\nu\kappa}$ becomes:

$$\chi_{\mu\tau\nu\kappa} = e^{ik_0\left(r_a - r_b\right)} \rho_X \rho_Y \left(\sum_{n=1}^{N} \sum_{p,q,r,s}^{w} \sum_{j,k,l,m}^{x,y,z} \Psi^{a,pq}_{n,\mu\tau,jk}\, \Psi^{b,rs*}_{n,\nu\kappa,lm}\, \mathcal{I}^{ab,pqrs}_{n,jklm} \right) \tag{46}$$

which conveys information about the remotely sensed area in wave frequency, observation angle, polarization, and scattering amplitude and phase.

2.2.9. Properties and Processes Contained in the Physics-Based Solution

Derived from vector wave equations satisfying Maxwell's equations subject to boundary conditions for stratified multi-layered media, result Equation 46 readily includes:

1. interferometric phase $e^{ik_0\left(r_a - r_b\right)}$ with azimuth decorrelation ρ_X (Zebker & Villasenor, 1992) and range decorrelation ρ_Y (Li & Goldstein, 1990)
2. frequency dispersion due to permittivity variations of constituents (e.g., air, ice, brine, seawater) in heterogeneous media (e.g., snow, sea ice)
3. shielding effect from the effective permittivities that include scattering effects in additional to the quasi-static parts
4. multi-layered configuration for N layers allowing the modeling of various types of snow-covered sea ice overcoming the weak profile requirement in the Wentzel-Kramers-Brillouin method
5. phases for multiple wave types $pqrs$ preserved in the correlation calculations for both upward and downward propagation directions consisting of 16 wave-type interaction combinations in an isotropic medium (e.g., snow with randomly oriented ice grains) and 256 combinations in a general anisotropic medium (e.g., columnar sea ice, sea ice with brine channels aligned in a preferential direction)
6. multiple interactions with interfaces in the multi-layered media (e.g., snow on sea ice over seawater) represented by coefficient Ψ's, including multiple reflections, refractions, transmissions, and birefringent effect or double refraction in a stratified anisotropic medium like first-year sea ice with brine inclusions having a preferential alignment in the C-axis crystallographic structure of the natural I_h ice grown on seawater
7. physical and structural properties of snow and sea ice described by $\mathcal{I}^{ab,pqrs}_{n,jklm}$ including permittivities of the medium constituents and scatterer geometry under various physical and environmental conditions in polar regions, and

10.1029/2021EA002191

8. all polarization combinations $\mu\tau\nu\kappa$ for fully polarimetric response of snow-covered sea ice to different incidence and scattered waves with different boundary conditions, scattering geometry, wave speed, and attenuation, including depolarization effects

The generalization of polarimetric interferometry given in Equation 46 can be readily and automatically reduced to bistatic scattering coefficients and backscattering coefficients when the observation points and wave directions are taken to the appropriate limits. In fact, polarimetric bistatic coefficient $\gamma_{\mu\tau\nu\kappa}$ in the polarimetric bistatic covariance matrix $\overline{\overline{C}}_{\gamma}$ and backscattering coefficient $\sigma_{\mu\tau\nu\kappa}$ in the polarimetric monostatic covariance matrix $\overline{\overline{C}}_{\sigma}$ can be derived from Equation 46 and the general covariance matrix $\overline{\overline{C}}_{\chi}$ defined by Equation 44:

$$\gamma_{\mu\tau\nu\kappa} = \lim_{a\to b}\chi_{\mu\tau\nu\kappa} \quad \Rightarrow \quad \overline{\overline{C}}_{\gamma} = \lim_{a\to b}\overline{\overline{C}}_{\chi} \tag{47}$$

$$\sigma_{\mu\tau\nu\kappa} = \lim_{b\to a}\chi_{\mu\tau\nu\kappa} \quad \Rightarrow \quad \overline{\overline{C}}_{\sigma} = \lim_{b\to a}\overline{\overline{C}}_{\chi} \tag{48}$$

Since snow-covered sea ice are reciprocal media, $\overline{\overline{C}}_{\sigma}$ in Equation 48 reduces to a 3×3 Hermitian matrix $\overline{\overline{C}}$ with nine complex elements for polarimetric backscatter coefficients given by Nghiem et al. (1990):

$$\overline{\overline{C}} = \begin{bmatrix} \sigma_{hhhh} & \sigma_{hhhv} & \sigma_{hhvv} \\ \sigma^{*}_{hhhv} & \sigma_{hvhv} & \sigma_{hvvv} \\ \sigma^{*}_{hhvv} & \sigma^{*}_{hvvv} & \sigma_{vvvv} \end{bmatrix} = \sigma \begin{bmatrix} 1 & \beta\sqrt{e} & \rho\sqrt{\gamma} \\ \beta^{*}\sqrt{e} & e & \xi\sqrt{\gamma e} \\ \rho^{*}\sqrt{\gamma} & \xi^{*}\sqrt{\gamma e} & \gamma \end{bmatrix} \tag{49}$$

where the symbol $*$ denotes the complex conjugate, and $\sigma = \sigma_{hhhh}$ is a normalization factor in the real-value co-polarized ratio γ, the real-value cross-polarized ratio e, and the complex-value correlation coefficients ρ, β, and ξ determined by the following equations:

$$\begin{gathered} \gamma = \frac{\sigma_{vvvv}}{\sigma}, e = \frac{\sigma_{hvhv}}{\sigma}, \rho = \frac{\sigma_{hhvv}}{\sigma\sqrt{\gamma}}, \\ \beta = \frac{\sigma_{hhhv}}{\sigma\sqrt{e}}, \text{and } \xi = \frac{\sigma_{hvvv}}{\sigma\sqrt{\gamma e}} \end{gathered} \tag{50}$$

In a short-hand notation, $\sigma_{hhhh} = \sigma_{\mathrm{HH}}$, $\sigma_{vvvv} = \sigma_{\mathrm{VV}}$, and $\sigma_{hvhv} = \sigma_{\mathrm{HV}}$, and $\sigma_{vhvh} = \sigma_{\mathrm{VH}}$, which are real numbers representing the radar power returns with different polarizations, either H for horizontal polarization or V for vertical polarization. In standard monostatic radar terminology, σ_{HH} and σ_{VV} are co-polarized backscatter coefficients, and σ_{HV} and σ_{VH} are cross-polarized backscatter coefficients.

2.2.10. Orientation Distribution

Scatterers like ice crystals in snow and air bubbles or brine inclusions in sea ice are not spherical and have different shapes with different characteristic scales in the three-dimensional (3D) space. The use of the local correlation function (Nghiem et al., 1995a) in the above formulation allows a statistical characterization of irregular shapes of scatterers in three dimensions with ellipsoidal correlation functions. Stronger scattering will result from scatterers with orientations such that larger cross-sections of the scatterers face toward the incidence field and observation directions.

The orientation also influences effective permittivities, changes the location of the scattering center, and thus varies the electromagnetic-wave phase. Depending on the preferential alignment of scatterers, the medium can be effectively anisotropic on the macroscopic scale even when permittivities of all individual constituents are isotropic. For scatterers with distributed orientation, such as brine inclusions in sea ice having a range of tilted angles with respect to the vertical direction or a random orientation in snow, field correlations in the calculations of effective permittivities and scattering coefficients involve conditional probability of Eulerian angles relating 3D principal coordinates of a local scatterer to the global coordinates by a rotation transformation matrix.

To account for effects of scatterer orientations, the probability density function of orientation $p_n(e_1, e_2, e_3)$ for the Eulerian angles e_1, e_2, and e_3 in region n is used in the calculations of effective permittivity and interferometric scattering with additional triple integrations for the three orientation angles, which can be carried out numerically following the method developed by Nghiem et al. (1995b).

2.2.11. Size and Shape Distributions

The relationship between scatterer size and scattering strength in snow-covered sea ice are highly nonlinear. For example, backscattering cross-section is proportional to the sixth power of the size in the Rayleigh regime, and follows the power law with different power indices in other scattering regimes. Therefore, the size distribution needs to be included in the theory, especially to account for a wide range of multiple microwave frequencies.

Scatterer shape determines the polarizability and impacts the wave propagation even in the lowest-order term. Moreover, scattering is strongly dependent on the shape; a spherical scatterer increases the cross-section if it is squeezed to an oblate spheroid for the same volume, or the cross-polarized return becomes larger if it is elongated to a tilted prolate spheroid. Using the method for electromagnetic modeling of sea ice by Nghiem et al. (1996, 1995a, 1995b), effects of size and shape distributions are characterized by size and shape probability density functions, which are allowed to be interrelated to account for thermodynamic metamorphoses in snow and sea ice.

2.2.12. Multiple Species

A heterogeneous layer in geophysical media is usually a mixture of various species of scatterers with different phases, like ice, brine, and air in snow-covered sea ice. Each species of the scatterers has different permittivity, orientation, size, and shape. Scattering, attenuation, and wave speed are dependent on the mixing fractions of different species.

Multiple species are modeled with a speciation approach which groups constituents with the same permittivity into a species to derive effective permittivities and scattering coefficients for the multiphase mixture. Each of the multiple species can also have distributed properties in orientation, size, and shape. These advances in the theory can include complex realistic properties of snow-covered sea ice under changing environmental conditions at the expense of complicated mathematical derivations and computations, which can be implemented with high-end computing facilities.

2.2.13. Rough Surfaces

Physical properties of snow-covered sea ice are further complicated by rough surface effects from both small-scale roughness (e.g., mm to cm scales at snow and ice interfaces) and large-scale roughness (e.g., hummocks due to differential melt, pressure ridges on sea ice, rafting of sea ice, etc.; Nghiem et al., 1995a). Rough surface scattering is modeled with a probability density $p(f)$ of the roughness profile that can be characterized by a height variance σ^2 and correlation length l_r to calculate surface scattering contribution at different frequencies and polarizations.

Moreover, for the surface scattering from an interface in multi-layered media, differences in attenuations and wave speeds and multiple interactions in the layers are accounted for, following the formulation by Nghiem et al. (1995a). The incidence wave is scattered by the rough interface (e.g., air-snow interface). The wave continues propagating into the snow layer where both the coherent and incoherent fields are scattered again by ice grains and the rough snow-ice interface. Part of the wave is transmitted into the underlying sea ice layer and is further scattered by scatterers (air bubbles and brine inclusions) in this layer and also by the rough interface between sea ice and seawater. The wave also reflects back toward the top interface and is scattered again by the inhomogeneities and the rough surfaces.

Processes of multiple scattering are complicated and involve surface scattering from above and below medium interfaces, multiple volume scattering in the heterogeneous layers, higher-order interactions between volume and surface scatterings, and wave propagation and attenuation in the multi-layered anisotropic media; all of which are included in the derivation of the overall resultant solution (Nghiem et al., 1995a).

2.3. Symmetry Group Theory

A fully polarimetric radar can measure radar scattering from geophysical media will all polarization combinations, resulting in many real and complex scattering coefficients as given Equations 46–48. Among a multitude of these polarimetric interferometric scattering coefficients, some terms may be primarily useful to retrieve sea ice DEM while other terms may introduce nonuniqueness and excessive noise. Thus, it is crucial to select which scattering coefficients to use and which ones to avoid. In this regard, the symmetry Group theory (Hamermesh, 1972) allows an examination of potential relationship among the various radar scattering coefficients for an effective selection of a primary set of radar measurements that preserve and contain the necessary information relevant to the measurement of sea ice DEM in this case.

Depending on symmetry conditions in snow-covered sea ice, not all scattering coefficients are independent as relationship exists among the polarimetric parameters (Nghiem et al., 1992, 1993). Thus, fully polarimetric measurements can be redundant and costly to implement in a satellite SAR system requiring an excessive data rate and data volume to be acquired across the vast expanse of polar sea ice over which many SAR scenes need to be processed. In particular, for OTASC, many TSX/TDX satellite SAR scenes were collected along thousand-km ground tracks and analyzing all covariance matrix terms is cumbersome and may potentially lead to confused results due to the nonuniqueness issue.

In the group theory, the symmetry is fundamentally determined by the mirror refection, axial rotation, and linear translation, which are invariant in the linear polarization basis regardless of the scattering mechanisms (Nghiem et al., 1993). The azimuthal symmetry group is a composition of the reflection and rotation symmetries, and is therefore consistent with the characteristics of both groups. In the azimuthal symmetry, sea ice backscatter is statistically similar on the left-hand side and the right-hand side with respect to a vertical plane oriented in any direction. Together with the reciprocity principle, the azimuthal symmetry group dictates that (Nghiem et al., 1992):

$$\sigma_{hvhv} = \left(\sigma_{hhhh} + \sigma_{vvvv} - 2\mathrm{Re}\,\sigma_{hhvv}\right)/4 \tag{51}$$

$$\text{or normalized as } e = (1 + \gamma - 2\mathrm{Re}\,\rho)/4 \tag{52}$$

Scattering from sea ice with randomly oriented scatterers in the ice volume and randomly oriented features on the ice surface is isotropic so that $\sigma_{HH} \approx \sigma_{VV}$ so that $\gamma \approx 1$, and $\mathrm{Im}\,\rho \approx 0$ so that $\rho \approx |\rho|$ (Nghiem et al., 1992). With the isotropic approximation condition, Equation 52 becomes $e \approx (1 + 1–2|\rho|)/4$, and therefore:

$$|\rho| \approx 1 - 2e \tag{53}$$

where $e = \sigma_{HV}/\sigma_{HH} = \sigma_{VH}/\sigma_{HH}$ for reciprocal media such as snow-cover sea ice. Equation 53 suggests that there can be a simple inverse relationship where the co-polarimetric signature magnitude $|\rho|$ decreases as the cross-polarization ratio e increases. Since e is larger for older and thicker sea ice (Nghiem et al., 1995b) with a higher ice surface elevation above the seawater level compared to that of younger and thinner sea ice, an inverse relation between $|\rho|$ and sea ice DEM may potentially exist so that $|\rho|$ can be selected and effectively utilized to develop a protocol to retrieve sea ice DEM from satellite SAR data.

3. Model Simulations

Physical structures and properties of sea ice are different in different polar regions. For Arctic sea ice, the approximate inverse relation in Equation 53 was observed in polarimetric SAR measurements over multi-year sea ice but not over first-year sea ice (Nghiem et al., 1993). Whether such relation may or may not exist for different classes of sea ice needs to be investigated for Antarctic sea ice because results for Arctic sea ice are not necessarily applicable to different sea ice conditions in the Antarctic. Thus, using the full electromagnetic model in Section 2, we carry out and present here a simulation of radar scattering coefficients based on physical parameters specifically pertaining to Antarctic snow-covered sea ice to select appropriate radar terms in order to develop a protocol for sea ice DEM retrieval in the Antarctic.

As a result of sea ice deformation processes, especially in the Western Weddell Sea driven by wind and wave dynamic forcing (Nghiem et al., 2016), sea ice becomes ridged, thickened, and elevated, leading to desalination through processes such as gravity drainage (Gow et al., 1987; Weeks & Ackley, 1982) that causes a loss

Table 1
Physical Characteristics of the Internal Ice and Snow Structures and the Dielectric Behaviors From the Published Literature

Sea ice	
Ice structure, crystallography	Gow et al. (1987), Tison et al. (2008), and Weeks and Ackley (1982)
Ice salinity	Gow et al. (1987), Tison et al. (2008), and Weeks and Ackley (1982)
Brine distribution profile	Gow et al. (1987), Tison et al. (2008), and Weeks and Ackley (1982)
Brine channels	Gow et al. (1987), Tison et al. (2008), and Weeks and Ackley (1982)
Brine inclusion volume	Cox and Weeks (1983), Tison et al. (2008), and Weeks and Ackley (1982)
Air inclusion volume	Cox and Weeks (1983) and Poe et al. (1974)
Basal ice layer above seawater	Tison et al. (2008)
Ice dielectric	Tiuri et al. (1984) and Vant et al. (1978)
Brine dielectric	Klein and Swift (1977) and Poe et al. (1972)
Sea ice effective dielectric	Nghiem et al. (1990, 1996, 1995a, 1993)
Snow cover	
Snow depth	Worby et al. (2008)
Snow loading	Ackley and Sullivan (1994) and Arndt et al. (2017)
Snow properties	Eicken et al. (1994) and Massom et al. (2001)
Ice dielectric	Tiuri et al. (1984) and Vant et al. (1978)
Effective dielectric of snow	Nghiem et al. (1990, 1995a, 1993)
Seawater	
Salinity structure	Foster and Carmack (1976)
Seawater dielectric	Klein and Swift (1977) and Poe et al. (1972)

of seawater brines in drainage channels where the voids become air inclusions with elongated shapes (Tison et al., 2008). As older sea ice is formed earlier and has a longer time to undergo deformation processes with a prolonged time for more extensive and intensive ridging for more elevated surface where more desalination occurs. Thus, the deformation effects are cumulative as younger and thinner sea ice can be deformed and continue being deformed as the sea ice becomes older and thicker. Also, thick sea ice can undergo severe ridging due to strong storm forcing in the Antarctic (Massom & Stammerjohn, 2010). These inter-related processes suggest a potential inverse relation between sea ice DEM and desalination for old, rough, and deformed sea ice. In contrast, younger and thinner sea ice in the Antarctic may undergo seawater flooding due to snow loading effects (Arndt et al., 2017), which happen more pervasively in the Antarctic compared to the conditions in the Arctic. As such, the young and thin sea ice can become furthermore salinated rather than desalinated, and thereby rendering the relation between ice DEM and desalination inapplicable. Based on realistic physical characteristics of the internal ice and snow structures and the dielectric behaviors from measurements reported in the published literature (see Table 1), the model simulation must capture these physical processes corresponding to different classes of sea ice in the Antarctic, which can be identified and mapped with satellite radar backscatter data (Nghiem et al., 2016).

To set up the model simulation, consider a layered-medium configuration (Figure 3) consisting of a snow cover on an upper sea ice layer, overlying of a lower basal sea ice layer. This basal saline layer contains brine inclusions with a high salinity in the profile transitioning toward the ice-seawater interface such as observed in the Western Weddell Sea (Tison et al., 2008). The salinity in the basal layer can be contributed from past flooding events on younger and thinner ice that becomes older and thicker so that brines in the upper ice volume above the sea level are drained down, and thereby further salinating the lower basal layer. The snow cover is modeled by a mean snow depth $d_s = 30$ cm for simplicity in understanding the polarimetric scattering processes in sea ice. For the objective of DEM retrieval over thick sea ice (1.5 to > 15 m), a 50% change in d_s may result in ~5% uncertainty in sea ice freeboard. The snow layer contains a fractional volume of 30% of randomly oriented ice grains (Nghiem et al., 1995b) with an oblate spheroidal shape characterized by scatterer correlation lengths of 0.9 and 1.5 mm. In the snow layer, the complex relative permittivity of ice grains is estimated to be $3.19 + i1.83 \times 10^{-3}$ with the real part from Vant et al. (1978) and the imaginary part from Tiuri et al. (1984) at the X-band frequency of 9.65 GHz

Synthetic Aperture Radar in space:
- TerraSAR-X/TanDEM-X (TSX/TDX)
- Operating frequency of TSX/TDX = 9.65 GHz
- Incidence angle centered at 34.9°

Atmosphere above the air-snow interface:
- Air dielectric dielectric (non-dispersive) = 1.0 + i0.0

Snow cover:
- Surface roughness with height standard deviation = 3.0×10^{-3} m and correlation length = 2.0×10^{-2} m
- Average snow depth = 30 cm
- Ice grains with randomly oriented oblate shape characterized by scatterer correlation lengths of 0.9×10^{-3} m and 1.5×10^{-3} m
- Ice grain dielectric = 3.19 + i(1.83×10^{-3}) at 9.65 GHz
- Air void dielectric (non-dispersive) = 1.0 + i0.0

Upper sea ice layer (desalinated):
- Surface roughness with height standard deviation = 5.0×10^{-3} m and correlation length is 2.0×10^{-2} m
- Background ice dielectric = 3.19 + i(1.83×10^{-3}) at 9.65 GHz
- Air inclusion dielectric (non-dispersive) = 1.0 + i0.0
- Air inclusions due to brine desalination with elongated shape having correlation lengths of 0.2×10^{-3} m and 2.0×10^{-2} m , and orientation angles randomly distributed in azimuth and tilted angles preferential distributed around 25° with respect to the vertical direction

Basal sea ice layer (salinated):
- Salinated sea ice layer above the ice-seawater interface
- Sea ice average effective dielectric = 6.73 + i4.33 at 9.65 GHz

Seawater:
- Seawater dielectric = 37.83 + i(41.48×10^{-3}) at 9.65 GHz

Figure 3. Configuration of snow-covered sea ice and parameters for model simulation (see references and the relevant text in Section 3).

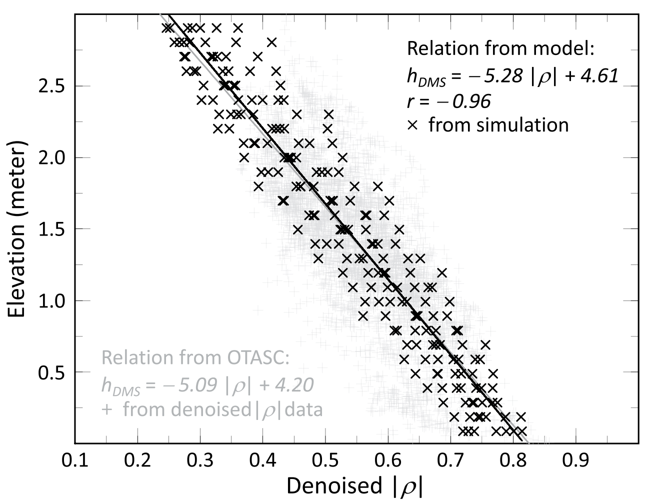

Figure 4. Comparison of sea ice elevation (h_{DMS}) vs. $|\rho|$ from model simulation results (×) with the regression line in black and from OTASC observations (+) with the regression line in brownish gray.

and incidence angle centered around 34.9° for TSX/TDX SAR (Krieger et al., 2007). At the snow-air interface, rough surface is characterized with a Gaussian distribution (Nghiem et al., 1995b) where the height standard deviation is 3.0×10^{-3} m and correlation length is 2.0×10^{-2} m to estimate the contribution from rough surface scattering in the total backscatter signatures.

The upper sea ice layer consists of an ice background medium (relative permittivity of $3.19 + i1.83 \times 10^{-3}$) and air inclusions (relative permittivity of $1.0 + i0.0$) due to the gravity desalination that forces seawater out of elongated brine channels with orientation angles randomly distributed in azimuth and a preferential alignment around 25° around the vertical direction. To be consistent with the elongated shape, air inclusions are prescribed in the model simulation with a prolate ellipsoidal form having correlation lengths of 0.2 mm in the minor axis and 2.0 cm in the major axis along the desalinated channels. In the basal salinated sea ice layer above the ice-seawater interface, where the fractional volume of brine inclusions can be high and range as much as 14%–26% (Tison et al., 2008) in the total sea ice volume, the average effective permittivity of the basal layer is $6.73 + i4.33$ at 9.65 GHz, obtained from a generalized dielectric mixing formulation that includes attenuation from both absorption loss and scattering loss (Nghiem et al., 1996). Due to the large imaginary part of $i4.33$, electromagnetic waves at 9.65 GHz are attenuated in the basal layer above the interface between sea ice and seawater that has a relative permittivity of $37.83 + i41.48 \times 10^{-3}$ (Klein & Swift, 1977). In the model simulation, rough-surface height standard deviation and correlation length are taken to be 5.0 mm and 7.0 cm respectively to account for the roughness at the interface between snow and sea ice.

The simulation is carried out over a range of sea ice freeboard from 0.2 to 3.6 m (d_{DMS}) for the upper sea ice layer above the sea level, where gravity desalination processes are effective especially for old, rough, and deformed sea ice conditions encountered over the Western Weddell Sea during the OTASC experiment (Nghiem et al., 2018). In this setting, $h_{\mathrm{DMS}} = d_{\mathrm{DMS}} + d_s$. For each step of 0.1 m in d_{DMS}, multiple scattered field ensembles are calculated. To assimilate the desalination process as sea ice becomes thicker and more elevated per Archimedes' principle, a function of $d_{\mathrm{DMS}} = 0.1 f_a - 3.0$ is used to directly relate the fractional volume of air inclusions f_a (in unit of 0.1%) to d_{DMS} (in unit of meter). Such gravity desalination processes in old, rough, and thick sea ice were reported (Gow et al., 1987). As ρ is determined by f_a, which in turn depends on sea ice elevation, ρ carries the information allowing the retrieval of sea ice elevation. The simulation includes statistic characterizations of d_{DMS} such as Gaussian, bell-shape, triangular-shape, and uniform distributions, which yield similar results as tested over a range of ± 0.3 m around each step of the mean value of d_{DMS} for the different distribution functions, where f_a takes on the specific value corresponding to each value of d_{DMS} in the ensemble calculations. This is to account for different elevations due to various surface features (e.g., pressure ridges, rubble ice, etc.) occurred in each radar footprint area ($\sim 10 \times 10$ m).

To examine how the model simulation for $|\rho|$ vs. sea ice elevation h_{DMS} may capture the behavior observed from OTASC field data, noise effects on $|\rho|$ in TSX/TDX SAR measurements are removed with a de-noised method (Huang et al., 2021; Nghiem et al., 1995b) to allow a consistent comparison of $|\rho|$ from experimental data and from model results that do not contain noise effects. As hinted by the symmetry group theory (Subsection 2.3), Figure 4 indeed reveals an inverse relation between $|\rho|$ and sea ice DEM in the model simulation with

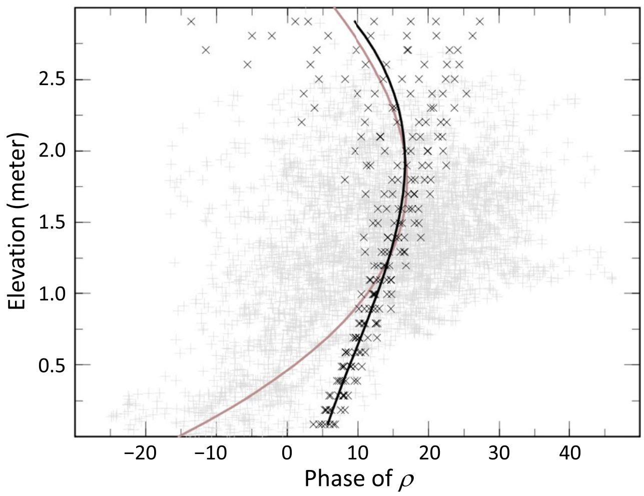

Figure 5. Comparison of sea ice elevation (h_{DMS}) vs. $\angle\rho$ from model simulation results (×) with the fitting curve in black and from OTASC observations (+) with the fitting curve in brownish gray.

a relation of $h_{\mathrm{DMS}} = -5.28|\rho| + 4.61$ (plotted with an offset of 0.3 in Figure 4) that nearly replicates the relation of $h_{\mathrm{DMS}} = -5.09|\rho| + 4.20$ from OTASC observations (Huang et al., 2021). The spread in $|\rho|$ are also similar with a standard deviation of 0.12 from simulation results, and 0.10 from OTASC data ranging from 0.35 to 0.86 for $|\rho|$ data obtained in the field campaign.

Regarding the phase of ρ (denoted by $\angle\rho$) presented in Figure 5, the comparison between simulation and experiment for h_{DMS} and $\angle\rho$ shows that both have a similar nonlinear trend for $h_{\mathrm{DMS}} > 1.3$ m. For smaller h_{DMS} (<1.3 m), both show an increasing trend, but the simulation curve has a steeper slope compared to that from OTASC. Also, results from both theoretical calculations and field observations have a large variability, and non-unique values of h_{DMS} in the cubic regression vs. $\angle\rho$ so that there can be double values of h_{DMS} for a given value of $\angle\rho$. In this comparison, the phase calibration for $\angle\rho$ has been verified (Huang et al., 2021). To overlay simulated results on measured data of $\angle\rho$ in Figure 5, the model $\angle\rho$ has been shifted by a small offset of 14°, which is within one standard deviation of $\angle\rho$ measured over sea ice during OTASC in the Western Weddell Sea (Huang et al., 2021).

4. Conclusions

For measurement of Antarctic sea ice DEM, a theory of radar polarimetric interferometry has been developed based on the analytic wave method fundamentally founded on the first principle of Maxwell's equations. As such, this theory allows the appropriate preservation of phase information that is imperative for radar polarimetric interferometry. Guided by the symmetry group theory to systematically examine a myriad of complex-valued terms in the fully polarimetric interferometric covariance matrix, the normalized co-polarized correlation coefficient ρ is suggested to have a potential use for retrieval of sea ice DEM. Model simulation results with properties of snow-covered sea ice pertaining to Antarctic sea ice conditions show an inverse relation between $|\rho|$ and sea ice DEM, which is hinted by the group theory and verified with OTASC observations.

As a key conclusion from results presented in this paper, a protocol is set up for sea ice DEM retrieval from satellite radar data acquired by X-band SAR such as TSX/TDX in the following steps: (a) process SAR data for noise subtraction from radar scattering coefficients, and for removing noise effects to obtained de-noised $|\rho|$; (b) use noise-subtracted scattering coefficients to classify sea ice and select the classes of rough and old sea ice with desalination from gravity drainage; (c) apply $|\rho|$ data in the inverse relation to retrieve sea ice DEM; and (d) validate retrieval results with OTASC observations. Note that ρ is a normalized polarimetric term per Equation 50, where the backscatter intensity is canceled out so that the magnitude of ρ varies between 0 and 1. This makes the DEM retrieval robust and less dependent on the absolute calibration of backscatter intensity.

Due to the nonlinearity and nonuniqueness, the phase term $\angle\rho$ will not improve and may actually degrade the estimation of sea ice DEM, which should be retrieved only with the $|\rho|$. Nevertheless, the interferometric phase term $e^{ik_0(r_a - r_b)}$ contains additional geometry information that can be used together with $|\rho|$ to achieve optimal results for sea ice DEM retrieval. The validated sea ice DEM derived from polarimetric interferometric SAR data will be valuable to obtain the DEM map over the same area of the corresponding sea ice class map across extensive areas of the satellite data coverage, so that a quantitative statistical characterization of large-scale sea ice roughness can be obtained from the DEM to associate to the corresponding classification of rough and old sea ice. This was not possible in the past as collocated and contemporaneous roughness and ice classification maps were not available to determine the large-scale roughness pertaining to each nomenclature of sea ice classes (WMO, 2014). Moreover, the DEM data product will enable a possible investigation of 3D characteristic patterns of sea ice DEM as directional forcing by winds and currents can form 3D directional features in the sea ice cover. These are to be presented in details in the next companion paper (Huang et al., 2021).

In this paper, we have focused on the specific objective of using the polarimetric interferometry model of sea ice to identify the specific radar terms to select and the terms to avoid in the protocol development for sea ice elevation retrieval in the Antarctic. Nevertheless, the model capabilities can be explored in other research efforts

10.1029/2021EA002191

to test the applicability for monitoring Arctic sea ice elevation, Great Lakes ice height, lake-ice level across the cold landscape, or other geophysical parameters in different environments of the Earth. Moreover, with the advent of multiple international SAR missions for Earth observations, the theory of radar polarimetric interferometry can be used to investigate the synergistic capabilities of SAR data at different frequencies, polarizations, incidence angles, etc., for science investigations in the cryosphere and elsewhere. Such studies will be useful to develop radar missions for cryospheric science in particular and for Earth science in general to select necessary rather than redundant radar measurements so that the satellite missions can be the most cost effective to be launched in the future.

Data Availability Statement

Data are at the data port https://dx.doi.org/10.21227/s7df-tq97.

Acknowledgments

The research carried out at the Jet Propulsion Laboratory (JPL), California Institute of Technology, was supported by the NASA Cryosphere Science Program. The authors acknowledge valuable discussions with Dr. Ted Maksym from the Woods Hole Oceanographic Institution, Prof. Stephen F. Ackley from the University of Texas at Antonio, and Prof. Jean-Louis Tission from the Université Libre de Bruxelles, regarding desalination, flooding, and properties of Antarctic sea ice, respectively. Moreover, the authors thanks our colleagues for their participations and collaborations in the OTASC efforts from the German Aerospace Center in Germany, the NASA Goddard Space Flight Center in USA, the University of Texas at San Antonio in USA, the Woods Hole Oceanographic Institution in USA, the Columbia University in USA, the University of Canterbury in New Zealand, the York University in Canada, the Alfred Wegener Institute in Germany, the U.S. National Ice Center in USA, the University of Washington in USA, and the University of Minnesota in USA.

References

Ackley, S. F., & Sullivan, C. W. (1994). Physical controls on the development and characteristics of Antarctic sea ice biological communities—A review and synthesis. *Deep-Sea Research*, *41*, 1583–1604. https://doi.org/10.1016/0967-0637(94)90062-0

Arndt, S., Meiners, K. M., Ricker, R., Krumpen, T., Katlein, C., & Nicolaus, M. (2017). Influence of snow depth and surface flooding on light transmission through Antarctic pack ice. *Journal of Geophysical Research: Oceans*, *122*(3), 2108–2119. https://doi.org/10.1002/2016jc012325

Barber, D. G., & Nghiem, S. V. (1999). The role of snow on the thermal dependence of microwave backscatter over sea ice. *Journal of Geophysical Research: Oceans*, *104*(C11), 25789–25803. https://doi.org/10.1029/1999jc900181

Brakenridge, G. R., Nghiem, S. V., Anderson, E., & Mic, R. (2017). Orbital microwave measurement of river discharge and ice status. *Water Resources Research*, *43*. https://doi.org/10.1029/2006WR005238

Cox, G. F. N., & Weeks, W. F. (1983). Equations for determining gas and brine volumes in sea ice. *Journal of Glaciology*, *29*(102), 306–316. https://doi.org/10.1017/s0022143000008364

Eicken, H., Lange, M. A., Hubberton, H.-W., & Wadhams, P. (1994). Characteristics and distribution patterns of snow and meteoric ice in the Weddell Sea and their contribution to the mass balance of sea ice. *Annales Geophysicae*, *12*(1), 80–93. https://doi.org/10.1007/s00585-994-0080-x

Foster, T. D., & Carmack, E. C. (1976). Temperature and salinity structure in Weddell Sea. *Journal of Physical Oceanography*, *6*(1), 36–44. https://doi.org/10.1175/1520-0485(1976)006<0036:TASSIT>2.0.CO;2

Gow, A. J., Ackley, S. F., Buck, K. R., & Golden, K. M. (1987). Physical and structural characteristics of Weddell Sea pack ice. *CRREL Report*, *14*, 1–70.

Guest, P. S., & Davidson, K. L. (1991). The aerodynamic roughness of different types of sea ice. *Journal of Geophysical Research: Oceans*, *96*(C3), 4709–4721. https://doi.org/10.1029/90jc02261

Hamermesh, M. (1972). *Group theory and its application to physical problems*. Reading, Massachusetts: Addison-Wesley.

Huang, L., Hajnsek, I., & Nghiem, S. V. (2021). Sea ice elevation in the western Weddell Sea, Antarctica: Observations from field campaign. *Journal of Geophysical Research: Oceans*. sumitted, TBD.

Jordan, A. K. (1998). Introduction to the special section on the electromagnetic properties of sea ice. *IEEE Transactions on Geoscience and Remote Sensing*, *36*(5), 1631–1632. https://doi.org/10.1109/tgrs.1998.718634

King, J. (2014). Climate science: A resolution of the Antarctic paradox. *Nature*, *505*(7484), 491–492. https://doi.org/10.1038/505491a

Klein, L., & Swift, C. (1977). An improved model for the dielectric constant of seawater at microwave frequencies. *IEEE Transactions on Antennas and Propagation*, *25*(1), 104–111. https://doi.org/10.1109/tap.1977.1141539

Krieger, G., Moreira, A., Fiedler, H., Hajnsek, I., Werner, M., Younis, M., & Zink, M. (2007). TanDEM-X: A satellite formation for high-resolution SAR interferometry. *IEEE Transactions on Geoscience and Remote Sensing*, *45*(11), 3317–3341. https://doi.org/10.1109/tgrs.2007.900693

Lee, J. K., & Kong, J. A. (1985). Electromagnetic wave scattering in a two-layer anisotropic random medium. *Journal of the Optical Society of America A: Optics, Image Science, and Vision*, *2*(12), 2171–2186. https://doi.org/10.1364/josaa.2.002171

Li, F. K., & Goldstein, R. M. (1990). Studies of multibaseline spaceborne interferometric synthetic aperture radars. *IEEE Transactions on Geoscience and Remote Sensing*, *28*(1), 88–97. https://doi.org/10.1109/36.45749

Liu, J., & Curry, J. (2011). *Resolving the paradox of Antarctic sea-ice growth*. Boston, MA, USA: American Meteorological Society.

Maksym, T., Stammerjohn, S. E., Ackley, S., & Massom, R. (2012). Antarctic sea ice—A polar opposite? *Oceanography*, *25*(3), 140–151. https://doi.org/10.5670/oceanog.2012.88

Martin, T., Tsamados, M., Schroeder, D., & Feltham, D. L. (2016). The impact of variable sea ice roughness on changes in Arctic ocean surface stress: A model study. *Journal of Geophysical Research: Oceans*, *121*(3), 1931–1952. https://doi.org/10.1002/2015jc011186

Massom, R. A., Eicken, H., Haas, C., Jeffries, M. O., Drinkwater, M. R., Sturm, M., et al. (2001). Snow on Antarctic sea ice. *Snow on Antarctic Sea Ice Review of Geophysics*, *39*(3), 413–445. https://doi.org/10.1029/2000rg000085

Massom, R. A., & Stammerjohn, S. E. (2010). Antarctic sea ice change and variability—Physical and ecological implications. *Polar Science*, *4*, 149–186. https://doi.org/10.1016/j.polar.2010.05.001

Mudaliar, S., & Lee, J. K. (1993). Modified radiative transfer theory in second-order backscattering coefficients of a two-layer random medium. *Radio Science*, *28*(4), 459–469. https://doi.org/10.1029/92rs02883

Nghiem, S. V., & Bertoia, C. (2001). Multi-polarization C-band SAR signatures of Arctic sea ice. *Canadian Journal of Remote Sensing, Focus Issue on Ice and Icebergs*, *2*(5), 387–402. https://doi.org/10.1080/07038992.2001.10854882

Nghiem, S. V., Borgeaud, M., Kong, J., & Shin, R. (1990). Polarimetric remote sensing of geophysical media with layer random medium model. *Progress in Electromagnetics Research*, *3*, 1–73. https://doi.org/10.2528/pier90030500

Nghiem, S. V., Busche, T., Kraus, T., Bachmann, M., Kurtz, N., Sonntag, J., et al. (2018). Remote sensing of Antarctic sea ice with coordinated aircraft and satellite data acquisitions. In *IGARSS 2018, IEEE International Geoscience and Remote Sensing Symposium*.

Nghiem, S. V., Kwok, R., Kong, J. A., Shin, R. T., Arcone, S. A., & Gow, A. J. (1996). An electrothermodynamic model with distributed properties for effective permittivities of sea ice. *Radio Science*, *31*(2), 297–311. https://doi.org/10.1029/95rs03429

Nghiem, S. V., Kwok, R., Yueh, S. H., & Drinkwater, M. (1995a). Polarimetric signatures of sea ice: 1. Theoretical model. *Journal of Geophysical Research: Oceans*, *100*(C7), 13665–13679. https://doi.org/10.1029/95jc00937

Nghiem, S. V., Kwok, R., Yueh, S. H., & Drinkwater, M. (1995b). Polarimetric signatures of sea ice: 2. Experimental observations. *Journal of Geophysical Research: Oceans*, *100*(C7), 13681–13698. https://doi.org/10.1029/95jc00938

Nghiem, S. V., Kwok, R., Yueh, S. H., Gow, A. J., Perovich, D. K., Kong, J. A., & Hsu, C. C. (1997). Evolution in polarimetric signatures of thin saline ice under constant growth. *Radio Science*, *32*(1), 127–151. https://doi.org/10.1029/96rs03051

Nghiem, S. V., Kwok, R., Yueh, S. H., Kong, J. A., Tassoudji, A. A., Hsu, C. C., & Shin, R. T. (1995). Polarimetric scattering from layered media with multiple species of scatterers. *Radio Science*, *30*(4), 835–852. https://doi.org/10.1029/95rs01247

Nghiem, S. V., Perovich, D. K., Polashenski, C., Lowe, S. T., Shah, R., Mannucci, A. J., et al. (2019). Polar sea ice thickness and melt pond fraction measurements with multi-frequency bistatic radar polarimetric and interferometric reflectometry. In *IGARSS 2019 IEEE International Geoscience and Remote Sensing Symposium*.

Nghiem, S. V., Rigor, I., Clemente-Colón, P., Neumann, G., & Li, P. (2016). Geophysical constraints on the Antarctic sea ice cover. *Remote Sensing of Environment*, *181*, 281–292. https://doi.org/10.1016/j.rse.2016.04.005

Nghiem, S. V., Steffen, K., Kwok, R., & Tsai, W.-Y. (2001). Detection of snow melt regions on the Greenland ice sheet using diurnal backscatter change. *Journal of Glaciology*, *47*(159), 539–547. https://doi.org/10.3189/172756501781831738

Nghiem, S. V., Yueh, S., Kwok, R., & Li, F. (1992). Symmetry properties in polarimetric remote sensing. *Radio Science*, *27*(05), 693–711. https://doi.org/10.1029/92rs01230

Nghiem, S. V., Yueh, S., Kwok, R., & Nguyen, D. (1993). Polarimetric remote sensing of geophysical medium structures. *Radio Science*, *28*(06), 1111–1130. https://doi.org/10.1029/93rs01376

Poe, G. A., Stogryn, A., & Edgerton, A. T. (1972). Microwave emission characteristics of sea ice. *Aerojet General Corp*. Rept. 1749R-2.

Poe, G. A., Strogryn, A., Edgerton, A. T., & Ramseier, R. O. (1974). Study of microwave emission properties of sea ice. *Aerojet General Corp*. Rept. 1804FR-1.

Ramsay, B., Flett, D., Andersen, H. S., Gill, R., Nghiem, S. V., & Li, P. (2004). Preparation for the operational use of RADARSAT-2 for ice monitoring. *Canadian Journal of Remote Sensing*, *30*(3), 415–423. https://doi.org/10.5589/m03-076

Tai, C.-T. (1971). *Dyadic Green's functions in electromagnetic theory*. Scranton. PA: International Textbook.

Tan, S., Zhu, J., Tsang, L., & Nghiem, S. V. (2017). Microwave signatures of snow cover using numerical Maxwell equations based on discrete dipole approximation in bicontinuous media and half space dyadic green's function. *IEEE Journal of Selected Topics in Applied Earth Observations and Remote Sensing*, *10*(11), 4686–4702. https://doi.org/10.1109/jstars.2017.2703602

Tison, J.-L., Worby, A., Delille, B., Brabant, F., Papadimitriou, S., Thomas, D., & Haas, C. (2008). Temporal evolution of decaying summer first-year sea ice in the Western Weddell Sea, Antarctica. *Deep-Sea Research Part II: Topical Studies in Oceanography*, *55*(8–9), 975–987. https://doi.org/10.1016/j.dsr2.2007.12.021

Tiuri, M., Sihvola, A., Nyfors, E., & Hallikaiken, M. (1984). The complex dielectric constant of snow at microwave frequencies. *IEEE Journal of Oceanic Engineering*, *9*(5), 377–382. https://doi.org/10.1109/joe.1984.1145645

Tsang, L., Kong, J. A., & Shin, R. T. (1985). *Theory of microwave remote sensing*. John Wiley & Sons.

Vant, M., Ramseier, R., & Makios, V. (1978). The complex-dielectric constant of sea ice at frequencies in the ranges 0.1–40 GHz. *Journal of Applied Physics*, *49*(3), 1264–1280. https://doi.org/10.1063/1.325018

Walsh, J. E. (2009). A comparison of Arctic and Antarctic climate change, present and future. *Antarctic Science*, *21*(3), 179–188. https://doi.org/10.1017/s0954102009001874

Weeks, W., & Ackley, S. F. (1982). The growth, structure, and properties of sea ice. *CRREL Monograph*, *82*(1), 1–130.

WMO (2014). World Meteorological Organization Sea Ice Nomenclature. *Fifth Session of JCOMM Expert Team on Sea Ice, WMO*, No. 259.

Worby, A. P., Markus, T., Steer, A. D., Lytle, V. I., & Massom, R. A. (2008). Evaluation of AMSR-E snow depth product over East Antarctic sea ice using in situ measurements and aerial photography. *Journal of Geophysical Research*, *113*(C05S94). https://doi.org/10.1029/2007JC004181

Zebker, H. A., & Villasenor, J. (1992). Decorrelation in interferometric radar echoes. *IEEE Transactions on Geoscience and Remote Sensing*, *30*(5), 950–959. https://doi.org/10.1109/36.175330